Monthly Notices
of the
ROYAL ASTRONOMICAL SOCIETY

MNRAS **493,** 5005–5023 (2020)
Advance Access publication 2020 February 18

doi:10.1093/mnras/staa495

TICs 167692429 and 220397947: the first compact hierarchical triple stars discovered with *TESS*

T. Borkovits,[1,2★] S. A. Rappaport,[3] T. Hajdu,[2,4] P. F. L. Maxted,[5] A. Pál,[2]
E. Forgács-Dajka,[6] P. Klagyivik[7] and T. Mitnyan[1]

[1] *Baja Astronomical Observatory of Szeged University, Szegedi út, Kt. 766, H-6500 Baja, Hungary*
[2] *Konkoly Observatory, Research Centre for Astronomy and Earth Sciences, Konkoly Thege Miklós út 15-17, H-1121 Budapest, Hungary*
[3] *Department of Physics, Kavli Institute for Astrophysics and Space Research, MIT, Cambridge, MA 02139, USA*
[4] *MTA CSFK Lendület Near-Field Cosmology Research Group, Konkoly Thege Miklós út 15-17, H-1121 Budapest, Hungary*
[5] *Astrophysics Group, Keele University, Staffordshire ST5 5BG, UK*
[6] *Eötvös Loránd University, Department of Astronomy, Pázmány Péter stny. 1/A, H-1118 Budapest, Hungary*
[7] *Deutsches Zentrum für Luft und Raumfahrt, Institut für Planetenforschung Rutherfordstrasse 2, D-12489 Berlin, Germany*

Accepted 2020 February 15. Received 2020 February 13; in original form 2019 December 23

ABSTRACT

We report the discovery and complex analyses of the first two compact hierarchical triple star systems discovered with *TESS* in or near its southern continuous viewing zone during Year 1. Both TICs 167692429 and 220397947 were previously unknown eclipsing binaries, and the presence of a third companion star was inferred from eclipse timing variations exhibiting signatures of strong third-body perturbations and, in the first system, also from eclipse depth variations. We carried out comprehensive analyses, including the simultaneous photodynamical modelling of *TESS* and archival ground-based WASP light curves, as well as eclipse timing variation curves. Also, for the first time, we included in the simultaneous fits multiple star spectral energy distribution data and theoretical PARSEC stellar isochrones, taking into account *Gaia* DR2 parallaxes and catalogued metallicities. We find that both systems have twin F-star binaries and a lower mass tertiary star. In the TIC 167692429 system, the inner binary is moderately inclined ($i_{\rm mut} = 27^{\circ}$) with respect to the outer orbit, and the binary versus outer (triple) orbital periods are 10.3 versus 331 d, respectively. The mutually inclined orbits cause a driven precession of the binary orbital plane that leads to the disappearance of binary eclipses for long intervals. In the case of TIC 220397947, the two orbital planes are more nearly aligned and the inner versus outer orbital periods are 3.5 and 77 d, respectively. In the absence of radial velocity observations, we were unable to calculate highly accurate masses and ages for the two systems. According to stellar isochrones TIC 167692429 might be either a pre-main sequence (MS) or an older post-MS system. In the case of TIC 220397947, our solution prefers a young pre-MS scenario.

Key words: binaries: eclipsing – binaries: close – stars: individual: TIC 167692429 – stars: individual: TIC220397947.

1 INTRODUCTION

Close, compact, hierarchical, multiple stellar systems, i.e. multiples at the lowest end of the outer period domain, comprise a small but continuously growing group of the triple and multiple star zoo. The significance of these most compact systems lies in the fact that they challenge or, at least probe, the alternative multiple star formation scenarios by their extreme properties. Furthermore, due to the relatively readily observable short-term dynamical interactions amongst the components, their dynamical as well as astrophysical properties can be explored with a high precision. For example, one key parameter that can be measured through the dynamical interactions in a compact triple system is the mutual inclination of the inner and outer orbits. This quantity is expected to be a primary tracer of the formation process(es) of triples and their later dynamical evolutions, leading to the present-day configurations of the systems (see e.g. Fabrycky & Tremaine 2007; Moe & Kratter 2018; Tokovinin & Moe 2020; and further references therein). Other, less emphasized parameters that can be deduced almost exclusively from the observations of short-term dynamical interactions of such systems are the orientations of the orbits relative to the intersections

---

★ E-mail: borko@electra.bajaobs.hu

Published by Oxford University Press on behalf of the Royal Astronomical Society

of their orbital planes (Borkovits et al. 2011). These parameters, the so-called dynamical arguments of periastron (i.e. the argument of periastron measured from the ascending node of the respective orbit relative to the invariable plane of the system instead of the tangential plane of the sky), have substantial importance for the long-term dynamical evolution of highly inclined multiples (see e.g. Ford, Kozinsky & Rasio 2000; Naoz 2016; and further references therein).

Before the advent of the era of space telescopes dedicated to searches for transiting extrasolar planets, only a very limited number of extremely compact triple or multiple stars were known. The preferred method for finding close tertiary components, before space missions, was the radial velocity (RV) measurements of known close binaries (discovered either by photometry or spectroscopy). Third stellar components orbiting eclipsing binaries (EB) could also be detected photometrically (and, frequently were), through eclipse timing variations (ETVs) due either to the light-traveltime effect (LTTE) or to direct third-body perturbations. Ground-based detection of *close* third stellar companions via ETVs, however, is less efficient for the following reasons. First, the LTTE is biased towards longer periods and more massive tertiaries, since the amplitude of an LTTE-caused ETV is $A_{\mathrm{LTTE}} \propto \frac{m_{\mathrm{C}}}{m_{\mathrm{ABC}}^{2/3}} P_2^{2/3}$. For the shortest outer period systems, this usually remains below the detection limit of ETVs found in strongly inhomogeneous ground-based eclipse timing observations. Secondly, the amplitude of the short-term dynamical perturbations on the ETVs scales with both the inner period and the inner to outer period ratio ($A_{\mathrm{dyn}} \propto P_1^2/P_2$); therefore, it becomes observable at the accuracy of ground-based measurements only for longer period EBs, which are unfavoured for ground-based photometry (see the discussion of Borkovits et al. 2003).

Whilst today's dedicated spectroscopic surveys lead continually to the discovery of new very compact multiple stellar systems (see e.g. most recently Tokovinin 2019, and further references therein), in the era of space photometry, photometric detection of these systems has become the dominant discovery mode. This breakthrough was largely due to the *Kepler* space telescope (Borucki et al. 2010) thanks to which the number of the closest compact triple (and in part, probably multiple) stellar systems has grown significantly over the last decade. Borkovits et al. (2016) have identified more than 200 triple star candidates amongst the ∼2900 EBs (Kirk et al. 2016) observed quasi-continuously by *Kepler* during its 4-yr-long primary mission. Eight of these triple candidates have outer periods less than 100 d, and an additional ∼27 systems were detected with outer periods less than 1 yr. Moreover, Borkovits et al. (2016) have shown that the absence of further very short outer period triples amongst *Kepler*'s EBs cannot be an observational selection effect. At least three additional very short outer period triple stars were detected in the fields of the *K2* mission; two of them, HD 144548 (Alonso et al. 2015) and EPIC 249432662 (Borkovits et al. 2019a), exhibit outer eclipses, whilst the third, HIP 41431, was discovered independently as a spectroscopic triple is indeed at least a 2+1+1 quadruple system (Borkovits et al. 2019b). Moreover, Hajdu et al. (2017) identified four triple-star candidates with outer periods probably less than 1 yr amongst EBs observed by the CoRoT spacecraft (Auvergne et al. 2009).

In this paper, we report the discovery and detailed analysis of the first two close, compact, hierarchical triple (or multiple) stellar systems, TICs 167692429 and 220397947 observed by the *TESS* spacecraft (Ricker et al. 2015). Both systems consist of previously unknown EBs composed of nearly equal mass ($q_1 > 0.9$) F-type stars (in the parlance of the binary- and multiple-star community: 'solar-type stars'). Both EBs have a detached configuration, and the orbital periods are $P_1 = 10.26$ and $P_1 = 3.55$ d for TICs 167692429 and 220397947, respectively. Both of them exhibit three-body perturbation-dominated, short-term ETVs, with periods $P_2 = 331$ d for TIC 167692429 and $P_2 = 77$ d for TIC 220397947. For TIC 167692429, the moderately eccentric EB exhibits eclipse depth variations with a clear signature of an outer periastron passage bump as a sign of an inclined eccentric tertiary. Both systems were observed with the WASP-South cameras (Hellier et al. 2011) between 2008 and 2014. These early light curves have been included into our analyses of the two systems. On the other hand, however, no RV measurements are available for these systems. Therefore, we use spectral energy distribution (SED) information, *Gaia* DR2 parallaxes, and theoretical PARSEC isochrones to constrain stellar masses and temperatures throughout the joint photodynamical analysis of the *TESS* and WASP light curves and ETV curves.

In Section 2, we describe all the available observational data, as well as their preparation for the analysis. Then, Section 3 provides a full explanation of the steps of the joint physical and dynamical modelling of the light- and ETV curves, SED, parallax and stellar isochrones. In Sections 4 and 5, we discuss the results from astrophysical and dynamical points of views. Finally, in Section 6, we draw conclusions from our findings.

2 OBSERVATIONAL DATA

The main observational characteristics of the two systems are tabulated in Table 1.

2.1 *TESS* observations

2.1.1 TIC 167692429

TIC 167692429 was observed by the *TESS* spacecraft (Ricker et al. 2015) during Year 1 in short cadence (SC) mode nearly continuously with the exception of Sector 5. Similar to other EBs in (or near), the continuous viewing zone (CVZ) we downloaded the calibrated SC data files for each sector from the MAST Portal.[1] The *TESS* light curve of TIC 167692429 is presented in Fig. 1.

As soon as the data from the first four sectors became available and were downloaded, we realized that ETVs of the primary and secondary eclipses exhibit non-linear, and mostly anticorrelated behaviours that are most probably of dynamical origin (see e.g. Borkovits et al. 2015). Data from this object over the next few sectors indicated that the eclipse depths were slightly increasing and that the primary and secondary ETVs, though converging weakly, did not show any characteristic non-linearity up to the second half of Sector 10. Then in Sector 11 both the eclipse depths and their timings changed dramatically hinting at the periastron passage of a third body in a significantly inclined and remarkably eccentric orbit.

This led us to collect all the observations and then carry out a complex photodynamical light curve and ETV analysis (see e.g. Borkovits et al. 2019a). For this purpose, we used the simple aperture photometry (SAP) data. We removed all data points flagged with non-zero values. Then we normalized the fluxes from each sector and concatenated them. Finally, we used the software package WŌTAN (Hippke et al. 2019) to detrend the light curves removing the instrumental effects. In order to check that we did not remove those light-curve features that might have arisen from binary star interactions (e.g. ellipsoidal variations, reflection effect, Doppler

---

[1] https://mast.stsci.edu/portal/Mashup/Clients/Mast/Portal.html

Table 1. Main characteristics of TICs 167692429 and 220397947.

Parameter		Value	
Identifiers	TIC	167692429	220397947
	TYC	8899-18-1	8515-663-1
	2MASS	06505184-6325519	04360354-5804334
Position	(J2015.5, *Gaia* DR2)	06:50:51.852, −63:25:51.76	04:36:03.537, −58:04:33.09
PM	μ_α, μ_δ (mas yr^{-1}, *Tycho*-2)	+4.6 ± 3.4, +16.1 ± 3.2	−4.1 ± 2.5, +28.2 ± 2.3
PM	μ_α, μ_δ (mas yr^{-1}, *Gaia* DR2)	+1.82 ± 0.06, +15.99 ± 0.05	+0.97 ± 0.04, +24.46 ± 0.05
Parallax	(mas, *Gaia* DR2)	1.41 ± 0.03	2.87 ± 0.02
$T_{\rm eff}$	(K, TIC-8)	6474 ± 117	6257 ± 131
	(K, *Gaia* DR2)	6342^{+220}_{-228}	6289^{+238}_{-158}
log *g*	(cgs, TIC-8)	3.48 ± 0.09	4.02 ± 0.09
Metallicity	[*M*/*H*]	−0.310 ± 0.046	−0.669 ± 0.061
Optical photometry[a]	*B*, *V* (mag)	11.408(21), 10.931(47)	11.301(28), 10.846(67)
	g', r', i' (mag)	..., 10.875(42), 10.784(33)	11.050(88), 10.793(41), 10.757(62)
Tycho-2 photometry[b]	B_T, V_T (mag)	11.491(64), 10.928(61)	11.585(76), 10.949(68)
Gaia photometry	*G*, B_P, R_P (mag)	10.8482(3), 11.1074(7), 10.4571(5)	10.7535(5), 11.0198(13), 10.3572(9)
Infrared photometry[c]	*J*, *H*, K_s (mag)	10.014(22), 9.805(21), 9.764(23)	9.913(23), 9.700(26), 9.598(20)
WISE photometry[d]	w_1, w_2 (mag)	9.723(23), 9.753(20)	9.567(21), 9.582(17)
Extinction	*E*(*B* − *V*) (mag)	0.064 ± 0.010	0.008 ± 0.010

Note. Sources of the SED information. [a]AAVSO Photometric All Sky Survey (APASS) DR9 (Henden et al. 2015), http://vizier.u-strasbg.fr/viz-bin/VizieR?-source = II/336/apass9; [b]*Tycho*-2 catalogue (Høg et al. 2000); [c]2MASS catalogue (Skrutskie et al. 2006); [d]*WISE* point source catalogue (Cutri et al. 2013). All the other data are taken directly from the *Gaia* DR2 (Gaia collaboration 2018) and TIC-8 (Stassun et al. 2018) catalogues. The original sources are listed in Section 2.4.

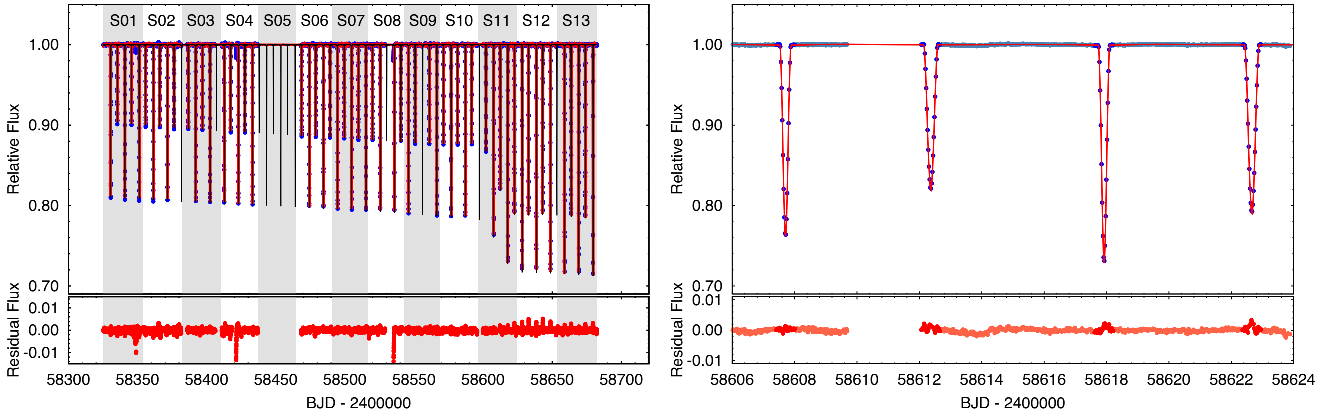

Figure 1. The *TESS* light curve of TIC 167692429. Instead of the full-resolution detrended SAP SC flux curve, we plot the 1800-s binned light curve that was used for the photodynamical analysis (see the text for details). *First row, upper panel*: The complete (Sectors 1–4, 6–13) light curve is plotted with blue dots. Red curve represents the cadence-time corrected photodynamical model solution (see Section 3). The thin black curves in the data gaps show the continuously sampled model light curve. Alternating grey and white stripes denote the consecutive *TESS* sectors. *Second row, upper panel:* An 18-d-long section of the light curve around the time of periastron passage of the third star. The dark blue circles in the ±0.3° phase-domain around each individual minimum represent the 1800-s binned flux values used for the photodynamical model, whilst the other out-of-eclipse data (not used in the modelling) are plotted as grey circles. The red curve is the cadence-time corrected photodynamical model solution; the residuals to the model are also shown in the bottom panels.

boosting), we made phase-folded, binned and averaged light curves both from the original and the detrended light curves, and adjusted the WŌTAN flattening parameter to such a value that the folded, binned, averaged detrended light curves qualitatively preserve the same out-of-eclipse features as the non-detrended ones.

2.1.2 TIC 220397947

This target was observed by *TESS* during Sectors 2–6, 8, 9, and 12. SC light curves are available only from Sectors 3, 4, 9, and 12. Similar to the other target above, SC light curves were downloaded from MAST Portal. For the long cadence (LC) light curves of those sectors where SC data were not available, we processed the *TESS* full-frame images using a convolution-based differential photometric pipeline, based on the various tasks of the FITSH package (Pál 2012). Namely, small stamps with a size of 64 × 64 pixels were extracted centred on the target source, and a combined stray light-free median image (created from 11 individual frames) was used as a reference for the image subtraction algorithm. The implemented image subtraction algorithm also accounts for the variations in the point spread functions (PSF) by fitting the appropriate convolution transformation. Whilst the actual variations in PSF are comparatively small, this step is important for removing the effect of the gradual drift in the light centroid positions caused by the differential velocity aberration. Instrumental fluxes were obtained using the appropriate equations provided by Pál (2009), whilst the zero-point reference was computed using the *Gaia* DR2 R_P magnitudes (Gaia collaboration 2016, 2018). This R_P magnitude is a rather accurate estimation due to the significant overlap of the *TESS* and *Gaia* passbands (Jordi et al. 2010; Ricker et al. 2015). We also downloaded LC light curves for Sectors 2–5 from the TESS Full Frame Image Portal[2] that hosts the data products from the pipeline of Oelkers & Stassun (2018). Whilst for the determination of the mid-eclipse times for each eclipse observed by *TESS*, we used both the LC and the SC data for the photodynamical analysis we used only the WŌTAN-detrended SC SAP light curve. A segment of the *TESS* light curve of TIC 220397947 is presented in the right-hand panel of Fig. 2.

2.2 WASP observations

Both TICs 167692429 and 220397947 are amongst the millions of stars that have been observed as part of the WASP survey. The survey is described in Pollacco et al. (2006) and Collier Cameron et al (2006). The WASP instruments each consist of an array of 8 cameras with Canon 200-mm f/1.8 lenses and 2k × 2k *e2V* CCD detectors providing images with a field of view of $7.8^\circ \times 7.8^\circ$ at an image scale of 13.7 arcsec pixel^{-1}. Images are obtained through a broad-band filter covering 400–700 nm. From July 2012, the WASP-South instrument was operated using 85-mm, f/1.2 lenses, and an r' filter. With these lenses the image scale is 33 arcsec pixel^{-1}. Fluxes are measured in an aperture with a radius of 48 arcsec for the 200-mm data, and 132 arcsec for the 85-mm data. The data are processed with the SYSRem algorithm (Tamuz, Mazeh & Zucker 2005) to remove instrumental effects.

Observations of TIC 167692429 were obtained simultaneously in two cameras on WASP-South over four observing seasons, from 2008 September 29 to 2012 March 23. During the four seasons of WASP observations, the target did not exhibit any eclipses; however, there is a clear dip in the measured flux with a depth of about 5.4 per cent and a duration of at least 1.17 d. There are no other dips of comparable depth and width in the WASP data.

Observations of TIC 220397947 were obtained simultaneously in two cameras on WASP-South over four observing seasons, from 2010 August 05 to 2014 December 19. A segment of the WASP light curve for TIC 220397947 is shown in the left-hand panel of Fig. 2.

2.3 ETV data

We determined the mid-time of each eclipse observed by *TESS* using both the SC and LC light curves, though for all further analyses, eclipse times obtained from the LC light curves were used only where SC data were unavailable. The method we used is described in detail by Borkovits et al. (2016). Note, that in the case of TIC 167692429, for the eclipse depth and duration variations during the 11 months of the *TESS* observations, in addition to the template fitting approach (Borkovits et al. 2016), we also found the eclipse times by fitting a parabola to each eclipse bottom. The two methods, however, resulted in very similar values, well within the estimated accuracies; therefore, we decided to use the first set of the ETV data obtained by using the method of Borkovits et al. (2016).

Regarding the WASP observations, TIC 167692429 did not exhibit eclipses during these measurements. By contrast, for TIC 220397947 several eclipses were observed during the four seasons of the WASP observations. Most of these eclipses, however, were unfortunately only partially covered and therefore, they do not lead to accurate eclipse timing determinations. Instead of the determination of the minima from a few average seasonal light curves, we found it to be more appropriate for our purposes to select the relatively better observed individual eclipses and determine their mid-eclipse times. Though these times of minima exhibit large scatter, they manifest a significant trend that leads us to the conclusion that TIC 220397947 might indeed be a 2+1+1-type quadruple system.

The times of minima of the two systems are listed in Tables 2 and 3, whilst the ETV curves are shown in Figs 3 and 4 for TICs 167692429 and 22039794, respectively.

2.4 SED data and *Gaia* results

Despite the relative brightnesses of both EBs, we have found only a very limited number of spectroscopic measurements in the literature (without any indications of the multiplicity of the sources). In particular, we found no RV data during our literature searches. As a consequence, no dynamically constrained masses are available for these systems. Furthermore, although the spectroscopic survey *TESS*-HERMES DR-1 (Sharma et al. 2018) gives spectroscopically determined effective temperatures for both systems, the surface gravities ($\log g$) derived from the same spectra clearly contradict our light-curve solutions. Therefore, we utilized a combination of SED data, PARSEC theoretical stellar isochrones (Bressan et al. 2012) and photodynamical model solutions (see Section 3) to determine the stellar masses and temperatures. In order to do this, we took compiled J, H, K_s, W_1, and W_2 magnitudes from the eighth version of the *TESS* Input Catalog (TIC-8; Stassun et al. 2018), which in turn subsumes photometric data from a large number of other photometric catalogues such as the Two-Micron All-sky Survey (2MASS; Skrutskie et al. 2006), and *Wide-field Infrared Survey Explorer* (*WISE*; Cutri et al. 2013). Moreover, we collected Johnson B, V, and Sloan g', r', i' magnitudes from the ninth data release of the AAVSO Photometric All-Sky Survey (APASS9; Henden et al. 2015) and also B_T, V_T magnitudes from *Tycho*-2 catalogue (Høg et al. 2000). Furthermore, we also utilized *Gaia* G, B_P, and R_P magnitudes, and trigonometric parallax $\varpi_{\rm DR2}$ taken from *Gaia* DR2 (Gaia collaboration 2018). Finally, we also took from TIC-8 the metallicity $[M/H]$ obtained from the spectroscopic survey *TESS*-HERMES DR-1 (Sharma et al. 2018).

We also consulted the *Gaia* DR2 and the *Hipparcos*/*Tycho* data bases for varying proper motion results. Both targets are included in the *Tycho*-2 catalogue (Høg et al. 2000). There are no significant proper motion changes during the 24.25-yr long baseline for our targets. For TIC 220397947, the proper motion errors are very close to the median value of the corresponding brightness range (see table 2 of Høg et al. 2000) and are consistent with the *Gaia* data within $2\,\sigma$. The errors for TIC 167692429 are slightly larger, which can be due to the smaller number of observations. In order to be able to include proper motion data into the analysis, we have to wait for the *Gaia* final data release that will contain all epoch and transit observations. All data listed above are presented in Table 1.

3 JOINT PHYSICAL AND DYNAMICAL MODELLING OF ALL THE AVAILABLE OBSERVATIONAL DATA

In our previous works (Borkovits et al. 2019a,b), we carried out joint, simultaneous spectrophotodynamical analyses of light, ETV, and RV curves of a number of compact hierarchical multiple systems. In those cases, there were available one or more RV curves

---

[2] https://filtergraph.com/tess_ffi/

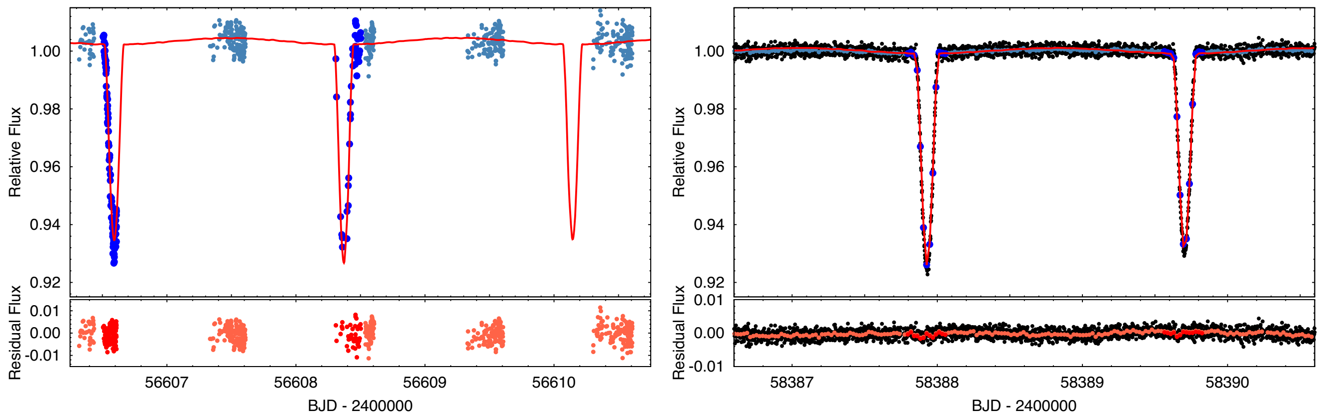

Figure 2. *TESS* and WASP light curves of TIC 220397947. *Upper left-hand panel*: A 4.5-d-long section of SWASP light curves with the photodynamical model solution. Dark blue circles show those observations that were used for photodynamical modelling, whilst the other, unmodelled, observations are plotted with light blue. Furthermore, the red curve represents the photodynamical model solution. *Upper right-hand panel:* A 4-d-long section of the light curve obtained by *TESS* during Sector 1 observations. Black dots represent the PDC-SAP SC fluxes. The dark blue circles in the $\pm 0\overset{\mathrm{p}}{.}04$ phase-domain around each individual minimum represent the 1800-s binned flux values used for the photodynamical model, whilst the other, similarly binned, out-of-eclipse data (not used for the modelling) are plotted by light blue circles. The red curve is the cadence-time corrected photodynamical model solution, the residuals to the model are also shown in the bottom panels.

Table 2. Times of minima of TIC 167692429.

BJD −2400 000	Cycle no.	Std. dev. (*d*)	BJD −2400 000	Cycle no.	Std. dev. (*d*)	BJD −2400 000	Cycle no.	Std. dev. (*d*)
58330.590372	0.0	0.000094	58468.715114	13.5	0.000075	58576.839937	24.0	0.000095
58335.331948	0.5	0.000079	58474.233865	14.0	0.000094	58581.580405	24.5	0.000074
58340.854210	1.0	0.000094	58478.975608	14.5	0.000080	58587.117373	25.0	0.000095
58345.591623	1.5	0.000083	58484.492996	15.0	0.000093	58591.833896	25.5	0.000067
58351.116444	2.0	0.000098	58489.236426	15.5	0.000065	58602.083879	26.5	0.000066
58355.851013	2.5	0.000088	58494.752538	16.0	0.000081	58607.708972	27.0	0.000087
58361.377729	3.0	0.000085	58499.497258	16.5	0.000066	58612.367185	27.5	0.000083
58366.111482	3.5	0.000097	58505.011331	17.0	0.000085	58617.921526	28.0	0.000097
58371.638409	4.0	0.000086	58509.758041	17.5	0.000067	58622.658055	28.5	0.000063
58376.371468	4.5	0.000073	58515.270790	18.0	0.000098	58628.203675	29.0	0.000179
58386.631345	5.5	0.000069	58520.018732	18.5	0.000070	58632.915717	29.5	0.000067
58392.158197	6.0	0.000095	58525.530013	19.0	0.000091	58638.489436	30.0	0.000103
58396.891705	6.5	0.000073	58535.789778	20.0	0.000106	58643.168928	30.5	0.000071
58402.418095	7.0	0.000084	58540.541099	20.5	0.000060	58648.763268	31.0	0.000108
58412.677795	8.0	0.000098	58546.049450	21.0	0.000099	58659.030530	32.0	0.000105
58417.412264	8.5	0.000072	58550.801516	21.5	0.000068	58663.681664	32.5	0.000070
58422.937174	9.0	0.000099	58561.062193	22.5	0.000075	58669.293862	33.0	0.000114
58427.672749	9.5	0.000082	58566.573032	23.0	0.000096	58673.939620	33.5	0.000058
58433.196453	10.0	0.000080	58571.322567	23.5	0.000069	58679.555548	34.0	0.000117

Note. Integer and half-integer cycle numbers refer to primary and secondary eclipses, respectively.

and, therefore, we were able to determine model-independent, dynamical masses for each component.[3]

In the present situation, however, in the absence of RV measurements we adopted an alternative, and astrophysical model-dependent method, inferring stellar masses, and temperatures from the combined modelling of light curves, ETVs, multiple SEDs, and stellar evolution models.

The combination of stellar isochrones and/or SED fits with an EB light-curve solver was introduced previously by, e.g., Devor & Charbonneau (2006), who pointed out that this method could lead to reasonable mass estimations for a large number of faint EBs observed during large photometric surveys. Later, Moe & Di Stefano (2013, 2015) analysed hundreds of EBs in the LMC in a similar manner. A related empirical method has also been used by Maxted & Hutcheon (2018) for characterizing EBs from the *K2* survey. Most recently, Windemuth et al. (2019) have determined physical and orbital parameters in such a manner for the detached EBs in the original *Kepler* field. Our method was mainly inspired by the paper of Windemuth et al. (2019), however, as far as we are aware, our efforts are the first to apply the SED+isochrone fitting method for multiple stellar systems.

For the combined modelling, we incorporated into the software package LIGHTCURVEFACTORY (see Borkovits et al. 2019a,b,

---

[3] For a dynamically interacting system, one needs only one component's mass (i.e. one RV amplitude), at least in theory, as the short-term dynamical interactions constrain the mass ratios strongly (see e.g. Rappaport et al. 2013; Borkovits et al. 2015).

Table 3. Times of minima of TIC 220397947.

BJD −2400 000	Cycle no.	Std. dev. (*d*)	BJD −2400 000	Cycle no.	Std. dev. (*d*)	BJD −2400 000	Cycle no.	Std. dev. (*d*)
55425.544843	– 833.0	0.000173	58371.938241	– 3.5	0.000135	58476.732255	26.0	0.000062
55432.647018	– 831.0	0.000425	58373.717958	– 3.0	0.000110	58478.504346	26.5	0.000148
55441.524433	– 828.5	0.000225	58375.491232	– 2.5	0.000046	58480.283904	27.0	0.000126
55496.586439	– 813.0	0.000940	58377.270547	– 2.0	0.000234	58482.056165	27.5	0.000180
55498.358609	– 812.5	0.000263	58379.043220	– 1.5	0.000111	58483.835542	28.0	0.001335
55514.343015	– 808.0	0.000196	58380.822856	– 1.0	0.000062	58485.607303	28.5	0.000347
55569.399842	– 792.5	0.000231	58384.376901	0.0	0.000115	58487.386712	29.0	0.000050
55585.385154	– 788.0	0.000224	58386.149994	0.5	0.000036	58489.158941	29.5	0.000212
55617.353910	– 779.0	0.000525	58387.929945	1.0	0.000032	58517.570308	37.5	0.000092
55782.523263	– 732.5	0.006381	58389.703234	1.5	0.000034	58519.349322	38.0	0.000339
55789.623554	– 730.5	0.004157	58391.483399	2.0	0.000029	58521.122208	38.5	0.000260
55798.509614	– 728.0	0.006379	58393.256496	2.5	0.000038	58522.901643	39.0	0.000104
55805.613433	– 726.0	0.000281	58395.036286	3.0	0.000045	58524.675031	39.5	0.000322
55814.487262	– 723.5	0.001839	58396.808493	3.5	0.000041	58526.454370	40.0	0.000143
55821.591741	– 721.5	0.000345	58398.588304	4.0	0.000043	58528.227732	40.5	0.000051
55830.475747	– 719.0	0.000319	58400.360410	4.5	0.000038	58535.332344	42.5	0.000118
55846.458539	– 714.5	0.000440	58402.139807	5.0	0.000043	58537.112508	43.0	0.000041
55862.446155	– 710.0	0.000396	58403.912264	5.5	0.000038	58538.886252	43.5	0.000060
55869.550282	– 708.0	0.000334	58405.691333	6.0	0.000036	58540.666174	44.0	0.000040
55871.320641	– 707.5	0.000496	58407.463464	6.5	0.000178	58545.993103	45.5	0.000043
55878.427212	– 705.5	0.000304	58409.242515	7.0	0.000204	58547.772304	46.0	0.000036
55885.527682	– 703.5	0.001080	58411.014691	7.5	0.000062	58549.545373	46.5	0.000040
55901.515712	– 699.0	0.000121	58412.794027	8.0	0.000039	58551.324561	47.0	0.000048
55917.497684	– 694.5	0.000238	58414.566148	8.5	0.000041	58553.097355	47.5	0.000031
55926.382119	– 692.0	0.000221	58416.345405	9.0	0.000037	58554.876377	48.0	0.000043
55933.485404	– 690.0	0.000601	58418.117360	9.5	0.000053	58558.428144	49.0	0.000030
55942.363865	– 687.5	0.000497	58421.669034	10.5	0.000058	58560.201140	49.5	0.000044
55974.328517	– 678.5	0.000494	58423.448354	11.0	0.000059	58561.979498	50.0	0.000039
56178.576926	– 621.0	0.000135	58425.219923	11.5	0.000044	58563.752076	50.5	0.000041
56242.512478	– 603.0	0.000085	58426.999079	12.0	0.000040	58565.530780	51.0	0.000036
56251.389203	– 600.5	0.000205	58428.771016	12.5	0.000044	58567.303422	51.5	0.000044
56258.493033	– 598.5	0.000160	58430.550484	13.0	0.000043	58627.689806	68.5	0.000054
56299.344637	– 587.0	0.000081	58432.322756	13.5	0.000038	58629.468525	69.0	0.000037
56306.448300	– 585.0	0.000131	58434.101671	14.0	0.000036	58631.241022	69.5	0.000048
56315.326180	– 582.5	0.000139	58435.874228	14.5	0.000044	58633.020688	70.0	0.000041
56347.295223	– 573.5	0.000197	58439.425783	15.5	0.000151	58634.793046	70.5	0.000039
56567.521093	– 511.5	0.000201	58441.205071	16.0	0.000106	58636.572329	71.0	0.000038
56574.624240	– 509.5	0.001192	58442.977939	16.5	0.000106	58638.344386	71.5	0.000035
56599.488418	– 502.5	0.000198	58444.757236	17.0	0.000055	58640.122770	72.0	0.000052
56606.593197	– 500.5	0.000347	58446.530362	17.5	0.000081	58641.895837	72.5	0.000048
56608.372742	– 500.0	0.000338	58448.310155	18.0	0.000159	58643.674949	73.0	0.000042
56622.579359	– 496.0	0.000190	58451.862607	19.0	0.000129	58645.447054	73.5	0.000042
56672.309088	– 482.0	0.000259	58453.635231	19.5	0.000199	58647.226031	74.0	0.000039
56711.382703	– 471.0	0.000793	58455.414842	20.0	0.000183	58648.998180	74.5	0.000050
58354.179002	– 8.5	0.000053	58457.187794	20.5	0.000121	58650.777500	75.0	0.000032
58355.957694	– 8.0	0.000159	58458.967508	21.0	0.001603	58652.549690	75.5	0.000037
58357.730220	– 7.5	0.000091	58460.741232	21.5	0.000095	–	–	–
58359.509098	– 7.0	0.000090	58462.521455	22.0	0.000124	–	–	–
58361.281906	– 6.5	0.000122	58469.628209	24.0	0.000054	–	–	–
58363.061012	– 6.0	0.000225	58471.401030	24.5	0.000064	–	–	–
58364.833939	– 5.5	0.000113	58473.180483	25.0	0.000125	–	–	–
58370.165529	– 4.0	0.000115	58474.952969	25.5	0.000072	–	–	–

Note. Integer and half-integer cycle numbers refer to primary and secondary eclipses, respectively. Most of the eclipses in the first column (cycle nos. −833.0 to −471.0) were observed in the WASP project, whilst the newer eclipse times (from cycle no. −8.5) determined from the *TESS* measurements.

and further references therein) the ability to handle tables of stellar isochrones and also to fit isochrone-generated SED data to the observed magnitudes making use of the known *Gaia* distance.

For this purpose, we generated machine readable PARSEC stellar isochrone grids (Bressan et al. 2012) via the web-based tool CMD 3.3.[4] The table(s) contain initial and actual stellar masses, bolometric luminosities ($\log L/\mathrm{L}_{\odot}$), effective temperatures ($\log T_{\mathrm{eff}}$), surface gravities ($\log g$), as well as absolute stellar

---

[4] http://stev.oapd.inaf.it/cgi-bin/cmd

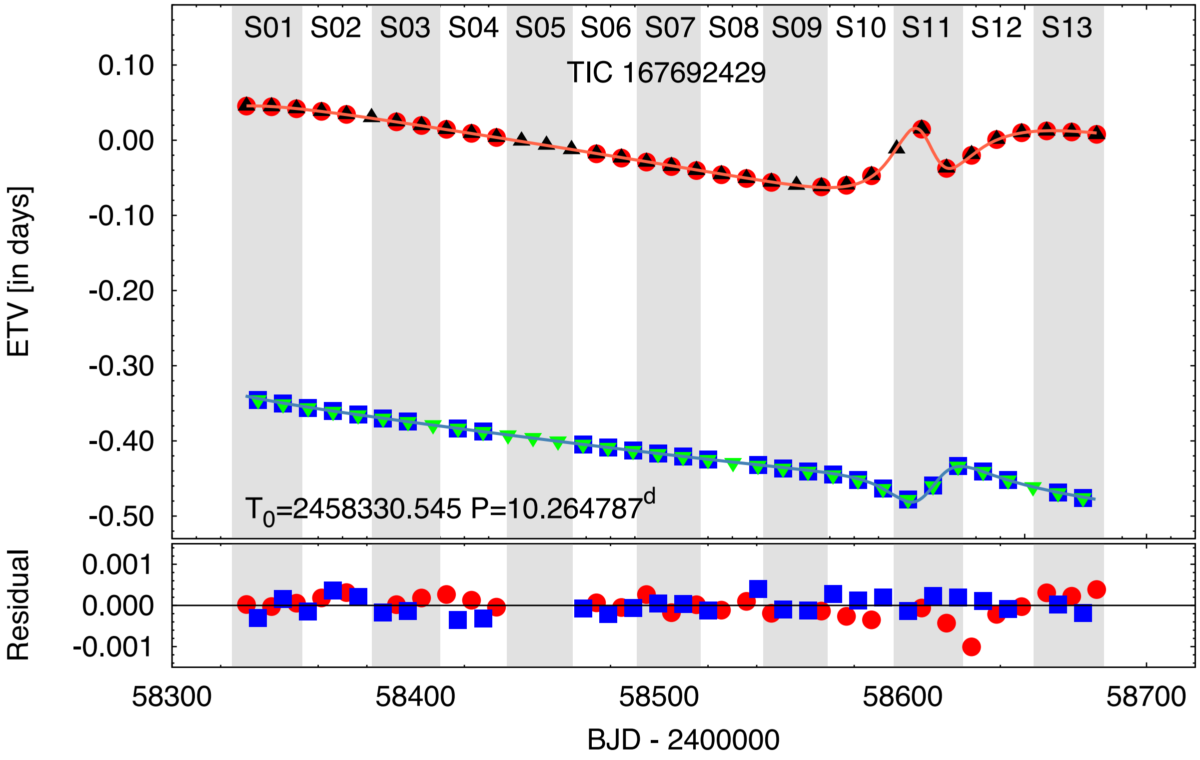

Figure 3. ETVs of TIC 167692429. Red circles and blue boxes represent the primary and secondary ETVs, respectively, calculated from the observed eclipse events, whilst black upward and green downward triangles show the corresponding primary and secondary ETV, determined from the photodynamical model solution. Furthermore, orange and light blue lines represent approximate analytical ETV models for the primary and secondary eclipses. The residuals of the observed versus photodynamically modelled ETVs are plotted in the bottom panel. As before, grey and white stripes denote the consecutive *TESS* sectors.

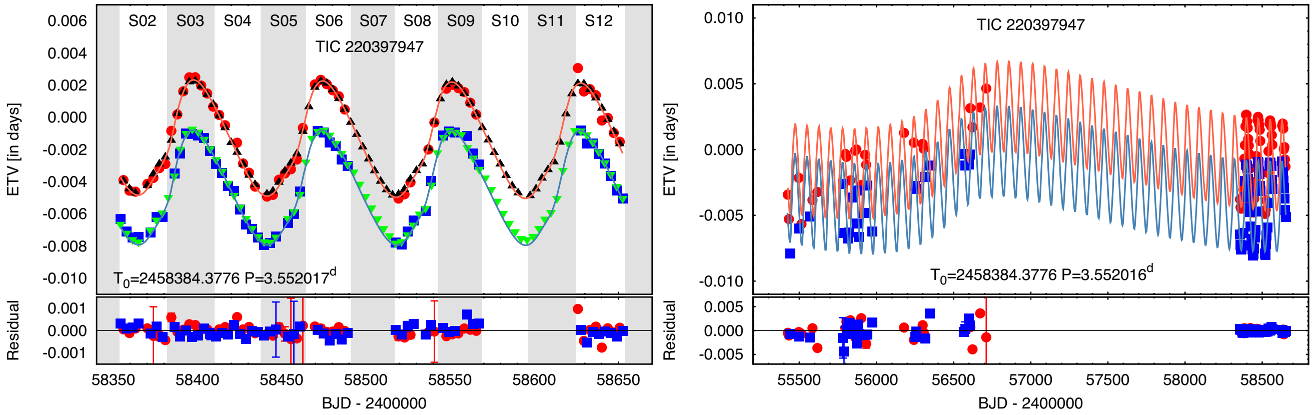

Figure 4. *Left-hand panel:* ETVs of TIC 220397947 during the 11 months of *TESS* observations. Red circles and blue boxes represent the primary and secondary ETVs, respectively, calculated from the observed eclipse events, whilst black upward and green downward triangles show the corresponding primary and secondary ETV, determined from the photodynamical model solution. Furthermore, orange and light blue lines represent approximate analytical ETV models for the primary and secondary eclipses. *Right-hand panel:* ETVs of TIC 220397947 from the beginning of the SWASP observations. As before, red circles and blue boxes represent the primary and secondary ETVs, but here orange and light blue lines connect the ETV points determined from the four-body dynamical modelling. The residuals of the observed versus photodynamically modelled ETVs are plotted in the bottom panels.

passband magnitudes in several photometric systems for the user selected grid of stellar metallicities and ages (log τ). LIGHTCURVEFACTORY now uses this table to calculate the above listed parameters (with trilinear interpolation) for the set of (mass, metallicity, age) values of the given star(s) under analysis. Then for the light-curve analysis part of the problem, the obtained effective temperatures and stellar radii can be used directly to generate the model light curve, whilst for the SED fitting the interpolated absolute passband magnitudes are converted to observed ones, taking into account the interstellar extinction and the distance of the system. To calculate the interstellar reddening, following the treatment of TIC-8 catalogue, we corrected for line-of-sight dust extinction assuming a standard exponential model for the dust with a scale height of 125 pc.

The main steps of our joint analysis were as follows:

(i) First, we carried out a joint photodynamical light curve and ETV analysis of both systems, applying a Markov Chain Monte Carlo (MCMC) parameter search. Initially, we modelled both systems as hierarchical triple stars.

Regarding the *TESS* SC light curves, in order to reduce the computational time we binned the 2-min cadence data, averaging them every half hour (i.e. 1800 s). Then, we narrowed the light curves to be modelled to ±0.03° and ±0.04° phase-domain regions around each eclipses, for TICs 167692429 and 220397947, respectively. Then these light curves were used in the photodynamical analysis (applying, of course an appropriate cadence time correction).

Having obtained the WASP observations of TIC 220397947, we realized that systematic departures from the expected (i.e. back-projected) eclipse times occurred one decade before the *TESS* observations, as well as a different eclipse period for the inner binary at that time. This was evident not only from an extended ETV analysis but also directly from the fitted WASP light curves that contain several only partially observed eclipses (and were not included into the ETV analysis). Therefore, we decided to model TIC 220397947 as a quadruple stellar system, having a 2+1+1 hierarchy. Therefore, besides the *TESS* SC observations, we included in the MCMC search another light-curve file, containing the similarly narrow sections around all the eclipses observed (mostly partially) with the WASP cameras. Furthermore, the times of minima deduced from the WASP observations were also added to the ETV curves to be fitted.

Similar to our previous work, in these runs we adjusted the following parameters:

(1) Three parameters related to the orbital elements of the inner binaries. For TIC 167692429, these parameters were as follows: the eccentricity (e_1), the phase of the secondary eclipse relative to the primary one ($\phi_{\mathrm{sec},1}$) that constrains the argument of periastron (ω_1, see Rappaport et al. 2017), and the inclination (i_1). For TIC 220397947, however, because of the very small eccentricity of the eclipsing pair, adjusting the more commonly used parameters $(e\sin\omega)_1$ and $(e\cos\omega)_1$ was found to be more practical.[5]

(2) Six parameters related to the orbital elements of the wide orbit of the third component: P_2 $(e\sin\omega)_2$, $(e\cos\omega)_2$, i_2, the time of periastron passage of star C along its wide orbit (τ_2), and the position angle of the node of the wide orbit (Ω_2).[6] Furthermore, in the case of the analysis runs for 2+1+1 quadruple representing TIC 220397947 a similar set of the orbital parameters (P_3, $[e\sin\omega]_3$, $[e\cos\omega]_3$, i_3, τ_3, and Ω_3) were adjusted for the outermost orbit.

(3) Two (or three) mass-related parameters: the mass ratios of the two (or three) orbits q_1, q_2 (and q_3).

(4) Finally, four (five) other parameters that are related (almost) exclusively to the light-curve solutions, as follows: the duration of the primary eclipse $(\Delta t)_{\mathrm{pri}}$ closest to epoch t_0 (which is an observable that is strongly connected to the sum of the fractional radii of stars A and B, i.e. scaled by the inner semi-major axis, see Rappaport et al. 2017), the ratio of the radii of stars A and B ($R_{\mathrm{B}}/R_{\mathrm{A}}$), and the temperature ratios of $T_{\mathrm{B}}/T_{\mathrm{A}}$, and the passband-dependent extra light(s) ℓ_{TESS} (and ℓ_{WASP}).

Turning to the other, light curve-related parameters, we applied a logarithmic limb-darkening law, where the coefficients were interpolated during each trial step from the pre-computed passband-dependent tables in the PHOEBE software (Prša & Zwitter 2005). The PHOEBE-based tables, in turn, were derived from the stellar atmospheric models of Castelli & Kurucz (2004). Due to the nearly spherical stellar shapes in both inner binaries, accurate settings of gravity darkening coefficients have no influence on the light-curve solution and, therefore, we simply adopted a fixed value of $g = 0.32$ which is appropriate for stars having a convective envelope according to the traditional model of Lucy (1967). Regarding the illumination/re-radiation effect, we found that it was quite negligible for the eclipsing pair of TIC 167692429, whilst it had a minor effect ($\lesssim 500$ ppm) for the light curve of TIC 220397947. Therefore, in order to save computing time, this effect was neglected. On the other hand, the Doppler-boosting effect (Loeb & Gaudi 2003; van Kerkwijk et al. 2010) that was also found to be negligible, but needs only very minor additional computational costs, was included into our model.

Moreover, in this first stage of analysis, we set the unadjusted primary masses (m_{A}) and effective temperatures (T_{A}) to the values given in the TIC. Here, we emphasize that at this stage the actual value of the masses and temperatures of the primaries played only a minor role, since we used these runs largely to constrain temperature ratios of the EBs, as well as the mass ratios of both the inner and outer binaries.

These runs revealed that both inner binaries were comprised of similar stars (i.e. both the inner mass and temperature ratios were found to be close to unity). Furthermore, from these light-curve solutions we were able to obtain reasonable estimates for the local surface gravities of each EB member star. For TIC 167692429, we found $\log g \approx 4.0-4.1$ for both stars, whilst for TIC 220397947 it was found to be $\log g \approx 4.1-4.3$ and $\approx 4.2-4.4$ for the primary and the secondary, respectively. These sets of the preliminary solutions have also shown that the additional outer stellar components are less massive stars that add only minor contributions to the systems' brightnesses and, therefore, can safely be omitted for the next step, i.e. for the preliminary SED fitting of the EBs.

(ii) In the next step, we fitted the observed passband magnitudes[7] (see Table 1) to SED models to find the approximate temperatures of the binary members. We fixed the inner mass ratios (q_1) to the values obtained previously in step (i), whilst a preliminary value

---

[5] Two other inner-orbit related parameters, namely the instantaneous orbital periods (P_1) and inferior conjunction time $(\mathcal{T}_0)_1$ of the secondary components of the inner binaries, i.e. the mid-primary-eclipse-times, were constrained with the use of the ETV curves in the manner explained in appendix A of Borkovits et al. (2019a), whilst the sixth orbital element, Ω_1, as irrelevant, was kept fixed at zero.

[6] As $\Omega_1 = 0°$ was assumed at epoch t_0 for all runs, Ω_2 set the initial trial value of the differences of the nodes (i.e. $\Delta\Omega$), which is the truly relevant parameter for dynamical modelling.

[7] Note for all of the SED-fitting processes we arbitrarily multiplied the small uncertainties of *Gaia*'s G, G_{BP}, G_{RP} magnitudes by a factor of 10 for two reasons. First, we wanted to avoid the extreme overdominance of these three magnitudes during the χ^2-optimization processes. The second reason was to counterbalance the expected larger systematic errors in the model SED magnitudes that were interpolated from the grid points. The uncertainties in the *Gaia* magnitudes are two orders of magnitude smaller than for the other SED points as well as compared to the systematic errors in the model SED. We therefore decided to adopt an uncertainty for the *Gaia* magnitudes that is the geometric mean between the actual *Gaia* magnitude uncertainties and the other uncertainties in this part of the problem. Substantially, smaller uncertainties for the *Gaia* points would render the other SED points of little value, whilst larger uncertainties for the *Gaia* magnitudes would fail to make use of their high precision.

for the primaries' masses were again taken from the TIC catalogue. With these stellar masses, we initialized an SED fitting procedure with the use of the built-in MCMC solver of our code. At this stage, we adjusted only the stellar age ($\log\tau$) parameter, whilst stellar metallicities and the interstellar extinction parameter $E(B-V)$ were kept fixed at their catalogue values. Moreover, the photometric distance was recalculated at each trial step so as to minimize $\chi^2_{\rm SED}$. In such a manner, we quickly found realistic $T_{\rm eff}$ values for the binary member's temperatures.

(iii) Then, using these temperatures, $\log g_{\rm A}$,[8] mass ratio (q_1), and the ratio of the radii ($r_{\rm B}/r_{\rm A}$) obtained in the previous light-curve fits, we searched the interpolated[9] PARSEC isochrone grids for those items (i.e. age, metallicity, and mass triplets) where both the primary's and secondary's $\log T_{\rm eff}$-s and $\log g$-s were simultaneously within a few per cent of the values obtained in the previous steps. These grid items (i.e. metallicity, age, and primary stellar mass values) were selected as the initial trial values for the first round of the combined SED (isochrone) and light-curve fits. Because we understood from step (i) that the outer stellar components yield only a minor contribution to the SED, in order to save substantial computational time at this point, we formed and fit folded light curves from the *TESS* SC observations of the two binaries. (Note, in the case of TIC 167692429 we used only the Sector 1–9 data, when the EB's light curve showed only minor variations in both eclipse shape and timing.) Then we binned these curves into 2000 uniform phase cells around the two eclipses and 500 cells in the out of eclipse sections. For each cell, we kept only the average of the individual flux values within the given cell.

These phased light curves were fitted simultaneously with the SED, using the corresponding, interpolated PARSEC isochrones. The initial values of the primary mass (m_1), stellar age ($\log\tau$), and metallicity ($[M/H]$) were taken from the above-mentioned parameter triplets. During the MCMC runs, these variables were adjusted together with the mass ratio (q_1), the orbital element-related parameters (see above), the third light (ℓ), the extinction parameter [$E(B-V)$], and the distance of the actual system (d). Regarding this last item, our treatment slightly departs from that of Windemuth et al. (2019). Those authors used Gaussian priors for the distance calculated from *Gaia*'s DR2 trigonometric parallax (and its uncertainty). We, however, used a uniform prior, initializing the distance variable with the *Gaia* trigonometric distance, but allowing practically any distance and, therefore, not penalizing any departures from the *Gaia* DR2 distances. The use of a uniform prior instead of a *Gaia* parallax-based Gaussian prior can be justified because at this stage we have not yet considered the other stellar components of these multiple star systems. And, since a minor part of the targets' total fluxes was thereby omitted, the binaries would be slightly fainter and, consequently, seemingly closer than the complete multiple systems.

As a conclusion for this stage of the analysis, we obtained dozens of light-curve solutions for a large variety of stellar age, metallicity, and mass triplets that were equally satisfactory or, quantitatively, where we found that $\chi^2 \lesssim 1.1\times\chi^2_{\rm min}$.

(iv) For the final stage in the analysis, our original intention was to select those solutions from the previous stage where the inferred photometric distance was within the 3σ uncertainty of the *Gaia* distance, and initialize the joint photodynamical light curve, ETV curve, SED, and PARSEC isochrone analysis with these parameters. However, we found that for TIC 167692429 all former stage solutions resulted in an incompatible distance with the *Gaia* result. Therefore, for this triple star, instead of the distances, we have chosen those solutions that were compatible with the metallicity given in the TIC. Oppositely, for TIC 220397947 we used the distances for the selection.

At this stage, the radii and effective temperatures of all three (four) stars were constrained by PARSEC isochrones. Apart from these, the adjusted parameters were the same as those listed in item (i) and item (iii) above. Moreover, in the case of TIC 220397947 we applied a Gaussian prior to the distance peaked at *Gaia*'s result; however, we set $\sigma = 3\sigma_{\rm Gaia}$, allowing for the inclusion of some systematic effects that might be present in the *Gaia* DR2 results due to the multiplicity of stars. On the other hand, for TIC 167692429 we kept a uniform prior on the distance.

A flow diagram of the entire fitting process is drawn in Fig. 5.

The orbital and astrophysical parameters derived from the photodynamical analysis are tabulated in Tables 4 and 5, and will be discussed in the subsequent Sections 4 and 5. The corresponding model light curves are presented in Figs 1 and 2, whilst the model ETV curves plotted against the observed ETVs is shown in Figs 3 and 4.

4 PHYSICAL PARAMETERS OF THE COMPONENTS

4.1 TIC 167692429

The preliminary stages of the analysis revealed that this system consists of non-MS components. The initial search amongst the PARSEC grids resulted in both pre- and post-MS isochrones. As was expected, we found that for lower metallicity values we obtained appropriate isochrones of lower mass stars (i.e. for a given initial mass, the more metal-rich a star is, the lower its effective temperature). Furthermore, we found, that for a given metallicity, the pre-MS isochrones, in general, belonged to more massive stars than the corresponding post-MS ones. We used isochrone grids in the metallicity range $-1.182985 \le [M/H] \le 0.595166$. Within this range, our preliminary search resulted in probable primary masses within $0.80\,{\rm M}_\odot \lesssim m_{\rm A} \lesssim 1.95\,{\rm M}_\odot$. As the effective temperatures of the EB members, and their relative radii as well as the mass ratio are relatively well known from the previous stages of the analysis, one can find that in this case, apart from additional light sources (i.e. the third component, being significantly less luminous), the total brightness of the system scales simply with the primary's mass according to $L_{\rm tot}\propto {m_{\rm A}}^{2/3}$. In such a way, there is a direct relation between the primary's mass and the (photometric) distance to the system (see the lower right-hand panel of Fig. 6).

As was mentioned in the previous section, in this way we have found a significant discrepancy between the trigonometric distance

---

[8] Strictly speaking, in the absence of a priori knowledge of the primary's mass, the photodynamical light-curve analysis results in only $\log g_{\rm A}* = \log g_{\rm A} - \frac{1}{3}\log m_{\rm A}$ (see e.g. Hajdu et al. 2017) from which value, however, $\log g_{\rm A}$ can be easily calculated for each individual trial mass. Then, the trivial relation of $\log g_{\rm B} = \log g_{\rm A} + \log q_1 - 2\log(r_{\rm B}/r_{\rm A})$ gives the surface gravity of the secondary.

[9] During this search process, the primary's actual mass ($m_{\rm A}$) was the only free parameter, which was increased evenly between $0.5\,{\rm M}_\odot$ and $3.0\,{\rm M}_\odot$ with a step size of $0.01\,{\rm M}_\odot$. At the same time, we calculated the secondary's mass from the mass ratio (q_1). Then for all the numerous doublets (metallicity, log age) in the PARSEC table, we calculated the other astrophysical parameters (i.e. $T_{\rm eff}$–s, $\log g$–s, and R–s) for both masses ($m_{\rm A}$ and $m_{\rm B}$), linearly interpolating between the previous and the next mass grid elements.

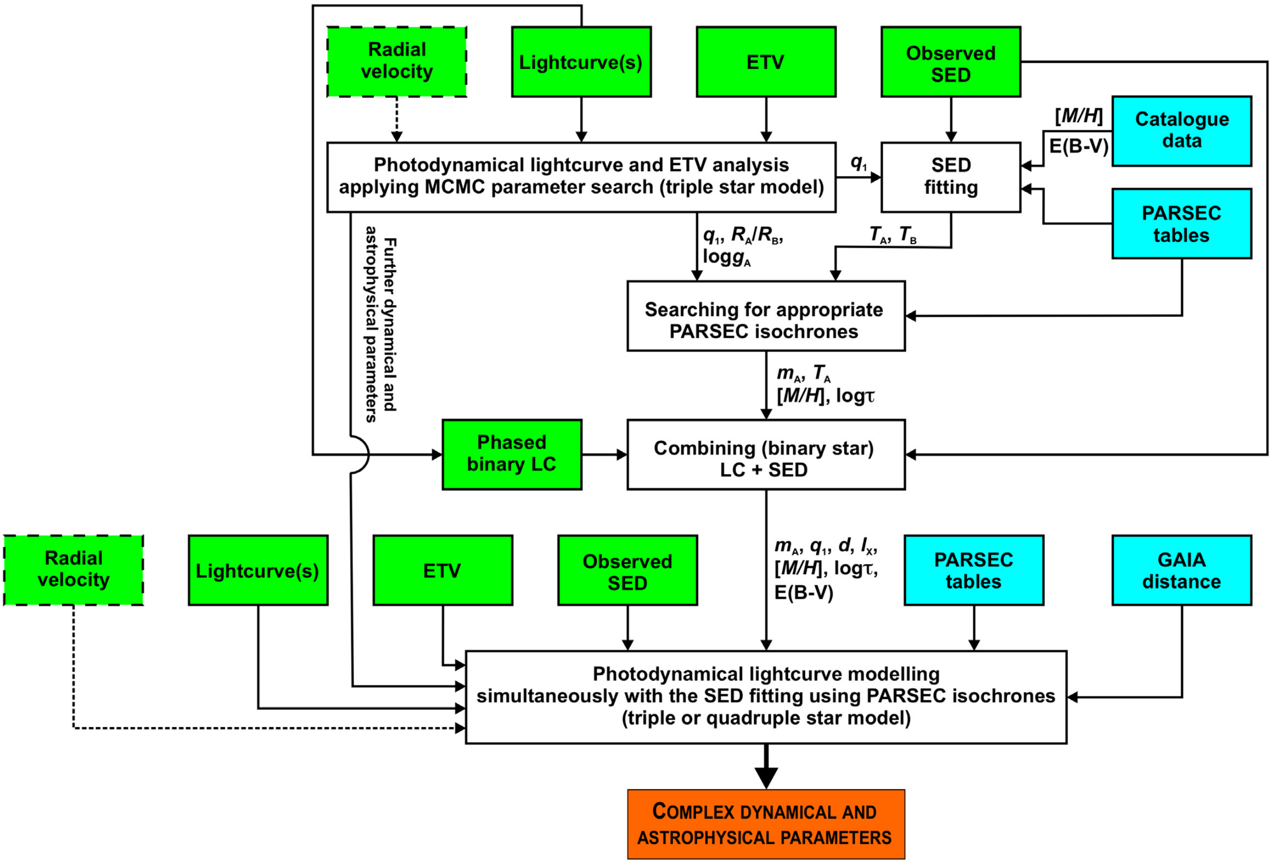

Figure 5. Flow diagram for the entire combined fitting analysis. We also list RV data in the rectangle with dashed borders. RV data were not used, however, in the present analysis because they were unavailable for these two systems; but, in principle, these can also be used in the combined analysis.

derived from the *Gaia* DR2 parallax, and the photometric one obtained from our joint analysis. For the most massive solutions (i.e. for $m_\mathrm{A} \sim 1.95\,\mathrm{M}_\odot$), our combined analysis – including the third star and the interstellar extinction – has resulted in a photometric parallax higher than the *Gaia* DR2 result at the $\approx 3\sigma$ level. Moreover, these most massive star scenarios belonged to the extreme metal-rich stellar isochrones (i. e. $[M/H] \approx 0.59$), whilst for TIC 167692429, the TIC lists $[M/H] = -0.309829 \pm 0.0462466$. Regarding only the metal-deficient (relative to the Sun) isochrones, we find primary masses $m_\mathrm{A} \lesssim 1.47\,\mathrm{M}_\odot$, which makes the distance discrepancy more significant.

This discrepancy perhaps can be resolved by the fact that the astrometric solutions used to produce the *Gaia* DR2 parallax do not take into account the wide outer binary nature of the systems. Similar or even much larger discrepancies have been reported, e.g., by Benedict, McArthur & Harrison (2018) who compared *HST* and *Gaia* Parallaxes and concluded that 8 per cent of their 'comparison sample of *Gaia* DR2 parallaxes have some issues with either target identification (high proper motion?) or binary motion.' In our case, the source of the discrepancy might be the $P_2 \approx 331$-d outer binary orbital motion. As one readily can find from Table 4, $a_2 \approx 1.4$ au. Taking into account that the outer mass ratio is $q_2 \approx 0.34$, the binary's centre of mass orbit has a semimajor axis of $a_\mathrm{AB} \approx 0.4$ au. According to our orbital solution, the major axis of the outer orbit viewed nearly edge-on practically coincides with the node ($i_2 \approx 86^\circ$; $\omega_2 \approx 0^\circ$); therefore, the projected, near 1-yr-period orbital motion of the photocentre is practically a straight-line segment having a length comparable ($\approx$40 per cent) to the trigonometric parallax, which might be co-measured with it.

In conclusion, unfortunately, in this case we cannot simply filter out the isochrones belonging to stellar masses that are inconsistent with the system's distance. Instead, we selected isochrones with $[M/H] \leq 0.0$, and looked for solutions within this metallicity constraint. We initiated several MCMC chains in both the post- and pre-MS domains. In the upper panels of Fig. 6, we show the m_A versus $\log\tau$ and m_A versus $[M/H]$ plots for both domains. These figures nicely illustrate the above-mentioned strong interdependencies amongst stellar masses, ages, and metallicities. Furthermore, one can see that the distributions of the appropriate stellar physical parameters are discontinuous, e.g. in the m_A versus $\log\tau$ and m_A versus $[M/H]$ planes.

This fact is also well illustrated in Fig. 7 where one can readily see the distinctly structured nature of the distribution for m_A. In particular, note the total lack of allowed solutions with primary mass $m_\mathrm{A} \sim 1.24\,\mathrm{M}_\odot$. We claim that this is a real physical effect and not simply an artefact caused by insufficient MCMC sampling. We justify this claim by noting that even in step (iii) of our complex process, i.e. whilst searching for PARSEC isochrone grid elements that a priori fulfil some preconditions characteristic of the given system (i.e. primary star temperature, mass and temperature ratios, etc.; see Section 3), we found only a small number of appropriate grid elements at these primary masses (relative to other masses). And later, when we initiated additional runs setting the input values of m_A, $[M/H]$, $\log\tau$ to lie directly in the gaps of Figs 6 and 7,

Table 4. Orbital and astrophysical parameters of TIC 167692429 from the joint photodynamical light curve, ETV, SED, and PARSEC isochrone solution. Besides the usual observational system of reference related angular orbital elements (ω, i, Ω), their counterparts in the system's invariable plane-related dynamical frame of reference are also given ($\omega^{\rm dyn}$, $i^{\rm dyn}$, $\Omega^{\rm dyn}$). Moreover, $i_{\rm m}$ denotes the mutual inclination of the two orbital planes, whilst $i_{\rm inv}$ and $\Omega_{\rm inv}$ give the position of the invariable plane with respect to the tangential plane of the sky (i.e. in the observational frame of reference). Columns 2–4 represent post-MS solutions, whilst columns 5–7 list the results of pre-MS solutions.

	Post-MS solution		Pre-MS solution	
	Orbital elements[a]			
	Subsystem		Subsystem	
	A–B	AB–C	A–B	AB–C
P (d)	10.26276 ± 0.00012	$331.50^{+0.28}_{-0.33}$	$10.26286^{+0.00010}_{-0.00011}$	331.45 ± 0.31
a (R$_\odot$)	$27.25^{+0.43}_{-0.41}$	$304.6^{+4.5}_{-4.9}$	$28.00^{+0.20}_{-0.24}$	$312.9^{+2.5}_{-2.3}$
e	$0.1734^{+0.0009}_{-0.0008}$	$0.55749^{+0.00072}_{-0.00071}$	0.1723 ± 0.0010	$0.55730^{+0.00081}_{-0.00082}$
ω (deg)	288.35 ± 0.11	$0.89^{+0.19}_{-0.17}$	288.47 ± 0.14	$0.79^{+0.17}_{-0.21}$
i (deg)	$85.731^{+0.036}_{-0.039}$	$85.68^{+0.22}_{-0.23}$	$85.796^{+0.057}_{-0.051}$	$85.50^{+0.34}_{-0.25}$
τ (BJD – 2400000)	$58320.6874^{+0.0030}_{-0.0031}$	58611.987 ± 0.078	$58320.6908^{+0.0039}_{-0.0038}$	$58611.902^{+0.099}_{-0.109}$
Ω (deg)	0.0	$-27.26^{+0.14}_{-0.13}$	0.0	-27.43 ± 0.16
$i_{\rm m}$ (deg)	$27.18^{+0.13}_{-0.14}$		27.36 ± 0.16	
$\omega^{\rm dyn}$ (deg)	$199.52^{+0.50}_{-0.53}$	$89.98^{+0.46}_{-0.47}$	$200.14^{+0.48}_{-0.75}$	$89.88^{+0.57}_{-0.63}$
$i^{\rm dyn}$ (deg)	$20.93^{+0.13}_{-0.14}$	$6.246^{+0.019}_{-0.018}$	21.12 ± 0.16	6.232 ± 0.020
$\Omega^{\rm dyn}$ (deg)	$270.44^{+0.48}_{-0.47}$	$90.44^{+0.48}_{-0.47}$	$269.98^{+0.66}_{-0.47}$	$89.98^{+0.66}_{-0.47}$
$i_{\rm inv}$ (deg)	$85.60^{+0.17}_{-0.18}$		$85.48^{+0.26}_{-0.21}$	
$\Omega_{\rm inv}$ (deg)	$-20.99^{+0.14}_{-0.13}$		-21.18 ± 0.16	
Mass ratio ($q = m_{\rm sec}/m_{\rm pri}$)	$1.005^{+0.011}_{-0.030}$	0.337 ± 0.002	0.993 ± 0.003	0.341 ± 0.003
$K_{\rm pri}$ (km s^{-1})	$68.46^{+0.99}_{-1.90}$	$14.07^{+0.23}_{-0.24}$	$69.63^{+0.53}_{-0.67}$	14.58 ± 0.14
$K_{\rm sec}$ (km s^{-1})	68.04 ± 0.65	$41.78^{+0.64}_{-0.61}$	$70.16^{+0.43}_{-0.57}$	$42.81^{+0.26}_{-0.37}$

	Stellar parameters					
	A	B	C	A	B	C
	Relative quantities[b]					
Fractional radius (R/a)	$0.0657^{+0.0034}_{-0.0016}$	$0.0667^{+0.0013}_{-0.0040}$	$0.00263^{+0.00008}_{-0.00009}$	0.0663 ± 0.0003	0.0660 ± 0.0004	$0.00350^{+0.00003}_{-0.00002}$
Fractional flux (in *TESS* band)	0.5316	0.3999	0.0576	0.4788	0.4567	0.0497
Fractional flux (in *SWASP* band)	0.5370	0.4170	0.0460	0.4873	0.4813	0.0314
	Physical quantities					
m (M$_\odot$)	$1.284^{+0.056}_{-0.043}$	$1.295^{+0.059}_{-0.076}$	$0.869^{+0.039}_{-0.043}$	$1.402^{+0.028}_{-0.035}$	$1.390^{+0.030}_{-0.037}$	$0.949^{+0.026}_{-0.021}$
R^b (R$_\odot$)	$1.800^{+0.075}_{-0.046}$	$1.822^{+0.043}_{-0.131}$	$0.803^{+0.036}_{-0.040}$	1.854 ± 0.020	$1.847^{+0.022}_{-0.026}$	1.094 ± 0.007
$T^b_{\rm eff}$ (K)	6544^{+20}_{-27}	6518^{+23}_{-34}	5597^{+34}_{-112}	6612^{+31}_{-28}	6531^{+26}_{-28}	4632^{+49}_{-41}
$L^b_{\rm bol}$ (L$_\odot$)	$5.33^{+0.49}_{-0.35}$	$5.32^{+0.32}_{-0.74}$	$0.57^{+0.06}_{-0.10}$	$5.90^{+0.12}_{-0.13}$	$5.574^{+0.16}_{-0.20}$	0.49 ± 0.02
$M^b_{\rm bol}$	$2.95^{+0.08}_{-0.10}$	$2.95^{+0.16}_{-0.06}$	$5.38^{+0.20}_{-0.10}$	2.84 ± 0.02	$2.90^{+0.04}_{-0.03}$	$5.53^{+0.04}_{-0.05}$
M^b_V	$2.95^{+0.08}_{-0.09}$	$2.96^{+0.17}_{-0.07}$	$5.48^{+0.22}_{-0.11}$	2.84 ± 0.03	$2.91^{+0.05}_{-0.04}$	$6.02^{+0.08}_{-0.09}$
$\log g^b$ (dex)	$4.04^{+0.02}_{-0.05}$	$4.03^{+0.04}_{-0.01}$	$4.57^{+0.02}_{-0.02}$	4.046 ± 0.004	4.047 ± 0.004	4.336 ± 0.008
log (age) (dex)	$9.464^{+0.056}_{-0.052}$			$7.028^{+0.030}_{-0.032}$		
$[M/H]$ (dex)	$-0.220^{+0.112}_{-0.059}$			$-0.207^{+0.103}_{-0.128}$		
$E(B-V)$ (mag)	$0.0533^{+0.0036}_{-0.0032}$			$0.0499^{+0.0033}_{-0.0049}$		
Extra light ℓ_4 (in *TESS* band)	$0.079^{+0.010}_{-0.012}$			$0.114^{+0.012}_{-0.013}$		
Extra light ℓ_4 (in *SWASP* band)	0.0			0.0		
$(M_V)^b_{\rm tot}$	$2.17^{+0.03}_{-0.07}$			2.09 ± 0.03		
Distance (pc)	552^{+14}_{-7}			574 ± 8		

[a] Instantaneous, osculating orbital elements, calculated for epoch $t_0 = 2458310.0000$ (BJD). [b] Interpolated from the PARSEC isochrones.

all these chains walked to the previously obtained islands of the a posteriori parameters.

The complex explanation for this fact is beyond the scope of this paper. Here, we simply refer to the evolutionary tracks formed from the PARSEC isochrones (see Fig. 8) where one can see that, e.g., in the case of the post-MS models for TIC 167692429 all three stars are located at very rapidly and steeply varying parts of their evolutionary tracks. We surmise that these 'kinks' in the evolutionary tracks might cause there to be no combinations of coeval evolutionary tracks of the three stars (with given mass ratios) for specific primary masses that would produce the required combination of stellar parameters that match the observed data.

In Table 4, we list our results for both the post-MS and pre-MS domain. As one can see, apart from the ambiguity discussed above

Table 5. Orbital and astrophysical parameters of TIC 220397947 from the joint photodynamical light curve, ETV, SED, and PARSEC isochrone solution. Besides the usual observational system of reference-related angular orbital elements (ω, i, Ω) their counterparts in the system's invariable plane related, dynamical frame of reference are also given (ω^{dyn}, i^{dyn}, Ω^{dyn}). Moreover, $(i_{\mathrm{m}})_{\mathrm{X-Y}}$ denotes the mutual inclination angle between orbits of subsystems X and Y, whilst i_{inv} and Ω_{inv} give the position of the invariable plane with respect to the tangential plane of the sky (i.e. in the observational frame of reference).

	Orbital elements^a		
	Subsystem		
	A–B	AB–C	ABC–D
P (d)	$3.55106^{+0.00004}_{-0.00005}$	$77.083^{+0.012}_{-0.010}$	2661^{+31}_{-29}
a ($\mathrm{R}_{\odot}$)	$12.836^{+0.037}_{-0.021}$	$107.544^{+0.958}_{-0.951}$	$1167.0^{+25.5}_{-8.9}$
e	$0.00105^{+0.00041}_{-0.00034}$	$0.2252^{+0.0195}_{-0.0124}$	$0.526^{+0.003}_{-0.006}$
ω (deg)	$319.441^{+13.90}_{-15.38}$	$340.90^{+0.43}_{-0.67}$	$198.10^{+0.50}_{-0.51}$
i (deg)	$82.283^{+0.266}_{-0.182}$	$82.669^{+0.274}_{-0.181}$	$88.624^{+2.4}_{-3.9}$
τ [BJD – 2400000]	$55411.8286^{+0.1559}_{-0.1353}$	$55378.648^{+0.037}_{-0.045}$	$53851.6^{+32.5}_{-32.0}$
Ω (deg)	0.0	$0.425^{+0.177}_{-0.263}$	$17.9^{+3.6}_{-3.8}$
$(i_{\mathrm{m}})_{\mathrm{AB\text{-}C,\,D}}$ (deg)	–	$0.57^{+0.24}_{-0.14}$	$18.9^{+3.3}_{-4.2}$
$(i_{\mathrm{m}})_{\mathrm{ABC\text{-}D}}$ (deg)	–	–	$18.4^{+3.3}_{-3.9}$
ω^{dyn} (deg)	$68.7^{+17.0}_{-13.9}$	$88.8^{+9.2}_{-13.5}$	$127.7^{+8.7}_{-12.3}$
i^{dyn} (deg)	$9.36^{+1.84}_{-2.76}$	$8.84^{+1.96}_{-2.45}$	$9.53^{+1.68}_{-1.60}$
Ω^{dyn} (deg)	$69.8^{+12.4}_{-8.3}$	$71.3^{+13.0}_{-9.1}$	$250.8^{+12.7}_{-8.9}$
i_{inv} (deg)	$85.45^{+1.42}_{-2.26}$		
Ω_{inv} (deg)	$8.86^{+2.02}_{-2.72}$		
Mass ratio ($q = m_{\mathrm{sec}}/m_{\mathrm{pri}}$)	$0.950^{+0.008}_{-0.012}$	$0.248^{+0.023}_{-0.028}$	$0.081^{+0.016}_{-0.012}$
K_{pri} ($\mathrm{km\,s^{-1}}$)	$88.328^{+0.318}_{-0.477}$	$14.296^{+1.140}_{-1.403}$	$1.959^{+0.369}_{-0.311}$
K_{sec} ($\mathrm{km\,s^{-1}}$)	$92.941^{+0.804}_{-0.550}$	$57.589^{+1.043}_{-0.752}$	$24.188^{+0.344}_{-0.251}$

	Stellar parameters			
	A	B	C	D
	Relative quantities			
Fractional radius (R/a)	$0.0942^{+0.0010}_{-0.0012}$	$0.0944^{+0.0012}_{-0.0012}$	$0.00746^{+0.00025}_{-0.00031}$	$0.00047^{+0.00003}_{-0.00003}$
Fractional flux (in *TESS* band)	0.5041	0.4643	0.0244	0.0044
Fractional flux (in SWASP band)	0.5233	0.4648	0.0101	0.0017
	Physical quantities^b			
m ($\mathrm{M}_{\odot}$)	$1.152^{+0.018}_{-0.009}$	$1.095^{+0.005}_{-0.006}$	$0.551^{+0.056}_{-0.065}$	$0.211^{+0.048}_{-0.037}$
R^b ($\mathrm{R}_{\odot}$)	$1.211^{+0.012}_{-0.012}$	$1.217^{+0.015}_{-0.014}$	$0.799^{+0.034}_{-0.040}$	$0.532^{+0.040}_{-0.041}$
T^b_{eff} (K)	6552^{+112}_{-44}	6281^{+39}_{-39}	3580^{+136}_{-71}	3077^{+86}_{-79}
L^b_{bol} ($\mathrm{L}_{\odot}$)	$2.43^{+0.12}_{-0.09}$	$2.07^{+0.05}_{-0.06}$	$0.09^{+0.02}_{-0.01}$	$0.023^{+0.009}_{-0.007}$
M^b_{bol}	$3.81^{+0.04}_{-0.05}$	$3.98^{+0.03}_{-0.03}$	$7.33^{+0.20}_{-0.26}$	$8.88^{+0.26}_{-0.25}$
M^b_V	$3.83^{+0.04}_{-0.05}$	$4.02^{+0.04}_{-0.03}$	$8.89^{+0.30}_{-0.46}$	$11.42^{+0.45}_{-0.43}$
$\log g^b$ (dex)	$4.33^{+0.01}_{-0.01}$	$4.31^{+0.01}_{-0.01}$	$4.37^{+0.01}_{-0.01}$	$4.31^{+0.01}_{-0.01}$
log (age) (dex)	$7.257^{+0.016}_{-0.008}$			
$[M/H]$ (dex)	$-0.3019^{+0.012}_{-0.051}$			
$E(B-V)$ (mag)	$0.0055^{+0.0074}_{-0.0030}$			
Extra light ℓ_5 (in *TESS* band)	$0.127^{+0.093}_{-0.053}$			
Extra light ℓ_5 (in SWASP band)	$0.034^{+0.029}_{-0.038}$			
$(M_V)^b_{\mathrm{tot}}$	$3.16^{+0.03}_{-0.04}$			
Distance (pc)	$349.8^{+6.3}_{-4.0}$			

[a] Instantaneous, osculating orbital elements, calculated for epoch $t_0 = 2455413.533621$ (BJD). [b] Interpolated from PARSEC isochrones.

related to the triplets of (mass, age, metallicity), the two solutions are very similar. In particular, the present orbital configuration and dynamics of our triple are very well determined by the observations and, in this sense, our results are conclusive. (The orbital and dynamical implications of the results will be discussed in the forthcoming Section 5.) From an astrophysical point of view, however, we cannot decide with certainty whether TIC 167692429 is a young pre-MS system or, conversely, it is an old evolved system. Though, the old, evolved scenario seems to be somewhat preferred in a statistical sense from our fits. What is certain is that the inner binary is comprised of two *F*-type twin stars ($q_1 = 0.99 \pm 0.02$), and the distant, third star is a less massive, G-type object. The locations of

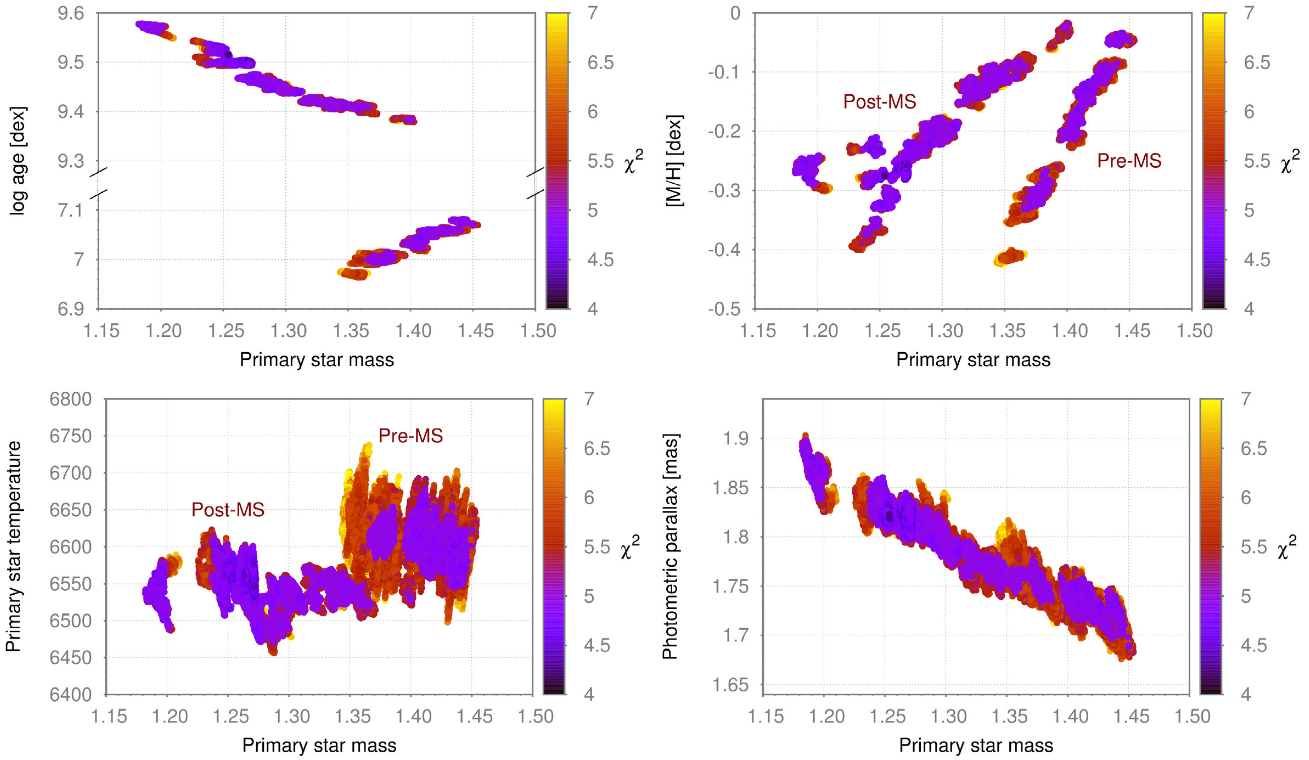

Figure 6. Correlation plots for TIC 167692429 amongst the primary star mass (m_A) and its age ($\log \tau$), metallicity ($[M/H]$), effective temperature ($T_\mathrm{eff,A}$), and photometric parallax (ϖ_phot). Upper left-hand and right-hand panels are $\log \tau$ and $[M/H]$ versus m_A, respectively. Lower left-hand and right-hand panels are $T_\mathrm{eff,A}$ and ϖ_phot versus m_A, respectively. The plotted points represent all the accepted MCMC trial steps both for the post-MS and pre-MS solutions. The colour scale represents the χ^2 value of each trial step and demonstrates that similarly low χ^2 value solutions can be obtained over a wide range of these parameters. Note the break in the *y*-axis in the upper left-hand panel.

the three stellar components on their appropriate PARSEC evolution tracks for both solutions are plotted in Fig. 8. It is interesting, at first glance, that the pre-MS solution results in hotter inner binary stars by $\Delta T_\mathrm{eff} \approx 50$–100 K relative to the post-MS solution (see, also, the lower left-hand panel of Fig. 6). This difference corresponds to 2–3σ uncertainties of both solutions. We interpret this finding by noting the fact that, in the case of the pre-MS solution, the third stellar component is found to be cooler by $\approx 1\,000$ K, while its luminosity remains nearly the same as for the post-MS case. Therefore, the members of the inner binary must be hotter to counterbalance the flux excess of the cooler tertiary on the infrared tail of the cumulative SED curve.

Despite the fact that our solutions have strongly degenerate dependencies on metallicities, masses, and ages, and the a posteriori distributions of some of the astrophysically most important parameters in the sample are far from Gaussian (see Fig. 7), we estimated their uncertainties formally as if they had normal distributions. Specifically, we have simply chosen to report the median value of each parameter as well as integrating the usual percentiles in both directions from the median value. In this simplistic way, we obtained e.g. 3–5 per cent 1σ uncertainties in the stellar masses.[10] The smaller uncertainties in the pre-MS case arise from the narrower mass region that can produce acceptable solutions within the investigated domain of metal-deficient isochrones, i.e. $-1.18 \leq [M/H] \leq 0.0$ (again see Fig. 6).

Our post- and pre-MS solutions give extinction-corrected photometric parallaxes of $\varpi_\mathrm{phot} = 1.81^{+0.02}_{-0.05}$ mas and $\varpi_\mathrm{phot} = 1.74 \pm 0.02$ mas, respectively, which are both substantially larger than *Gaia*'s $\varpi_\mathrm{DR2} = 1.41 \pm 0.03$ mas. One can expect a resolution of this discrepancy when the DR3 edition of the binary-motion-corrected *Gaia* results is released in 2021.

Returning to the mass–age relations (Fig. 6), one can see that primary star masses in the range of $1.35\,\mathrm{M}_\odot \lesssim m_\mathrm{A} \lesssim 1.41\,\mathrm{M}_\odot$ might pertain to both pre- and post-MS solutions. As a consequence, if some future RV observations yield dynamical masses outside the above mass range, one will be able to decide immediately, whether the post- or the pre-MS scenario is valid. A similar statement can be made in the context of the expected very accurate *Gaia* DR3 distances. A trigonometric parallax of $\varpi_\mathrm{DR3} \gtrsim 1.80$ mas would clearly imply an evolved scenario, while $\varpi_\mathrm{DR3} \lesssim 1.70$ mas is expected to be found only for the case of the pre-MS solutions.

4.2 TIC 220397947

As discussed above, for this system we took into account the *Gaia* DR2 parallax, applying a Gaussian prior to the photometrically obtained parallax. We found that in the neighbourhood of the catalogue's metallicity values of $[M/H] = -0.668558 \pm 0.0612805$ our solutions led to photometric parallaxes that were too large

---

[10] Note Moe & Di Stefano (2015) have estimated similar uncertainties using a quite similar method to obtain fundamental parameters from combined light curve and isochrone analysis of EBs of the LMC.

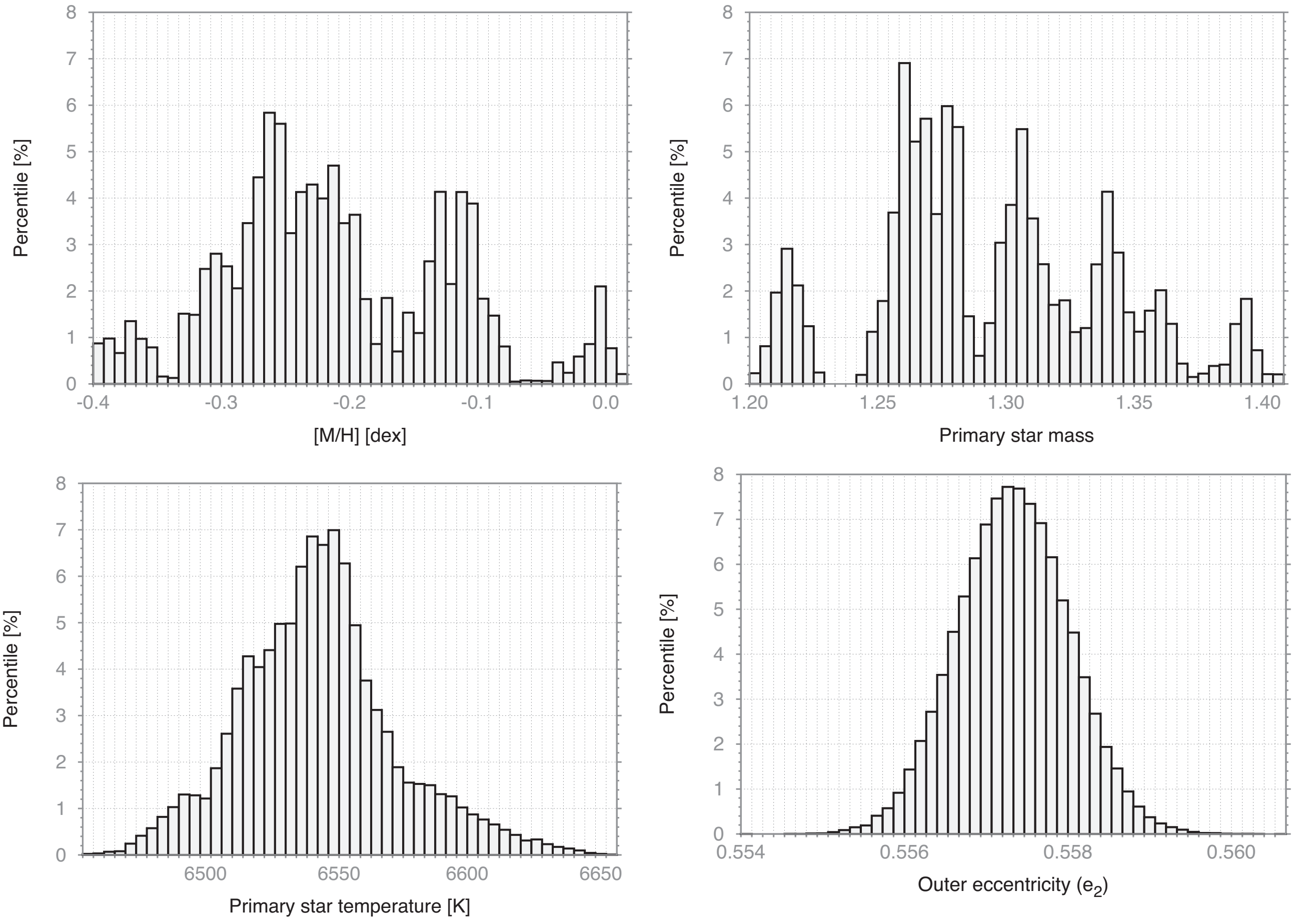

Figure 7. Histogram plots illustrating the distributions of some parameters of the TIC 167692429 system for the post-MS models. Upper row displays the highly non-Gaussian distributions of the primary star's mass ($m_{\rm A}$) and metallicity ($[M/H]$). The bottom row shows the close to Gaussian distribution of the primary star's effective temperature ($T_{\rm eff,A}$), and the practically perfect Gaussian distribution of the outer eccentricity (e_2). These distributions were chosen to be illustrative of similar distributions for the majority of the orbital elements.

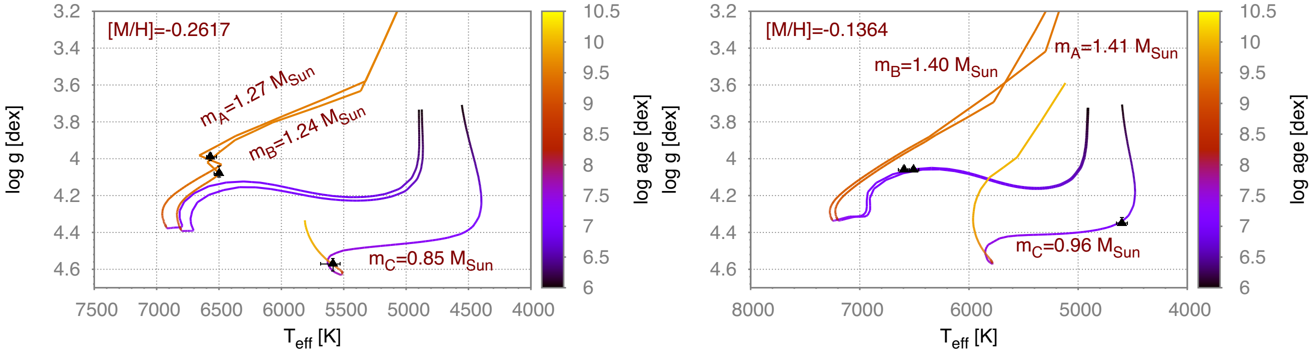

Figure 8. $T_{\rm eff}$ versus $\log g$ PARSEC evolutionary tracks for the three components of TIC 167692429 for both the evolved (left-hand panel) and pre-MS scenarios (right-hand panel). The colour scale denotes the age ($\log \tau$) of the stars at any given point along their evolution tracks. Black triangles mark the present locations of the three stars at ages $\log \tau \approx 9.50$ and $\log \tau \approx 7.05$ in the left-hand and right-hand panels, respectively.

compared to *Gaia*'s result and, therefore, these strongly metal deficient solutions were highly penalized by the Gaussian prior. We found that moderately metal-deficient isochrones offer solutions that are in accord with the *Gaia* distance. A bit surprisingly, however, our MCMC parameter searches favoured very young stellar ages, i.e. pre-MS star solutions instead of evolved star scenarios (see Table 5 and Fig. 9, as well). In our understanding, this arises from that fact that the inner mass ratio (q_1), which is determined chiefly by the ETV curve, and the temperature ratio ($T_{\rm eff,\,B}/T_{\rm eff,\,A}$), which primarily sets the primary-to-secondary eclipse depth ratio, were slightly discrepant for the evolved star solutions. In other words, in the case of post-MS solutions, when the mass ratio (q_1) was found from the ETV fit, the secondary eclipses were too deep relative to the primary ones (i.e. $\chi^2_{\rm LC}$ became larger), while for the

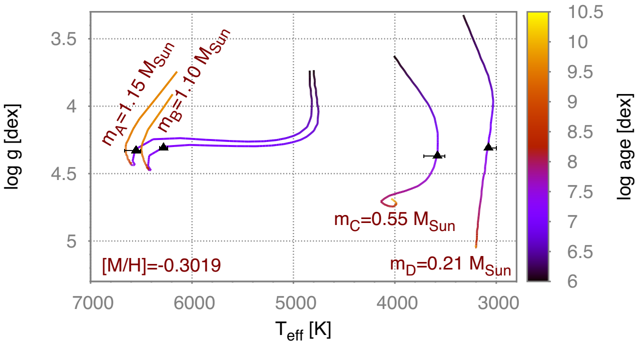

Figure 9. $T_{\rm eff}$ versus $\log g$ PARSEC evolutionary tracks for the four components of TIC 220397947 according to our pre-MS model. The colour scale denotes the age ($\log \tau$) of the stars at any point along their evolution tracks. Black triangles mark the present locations of the four stars at age $\log \tau \approx 7.26$.

correct temperature ratio and, therefore proper eclipse depths, the ETV residuals were too large (i.e. $\chi^2_{\rm ETV}$ penalized the solution).

Note, the circular inner orbit does not contradict the inferred very young age of the system. As was shown by Zahn & Bouchet (1989), orbits of late-type stars with $P \lesssim 7-8$ d are expected to circularize by the end of their first million years of pre-MS evolution.

5 ORBITAL PROPERTIES AND DYNAMICAL EVOLUTION

In contrast to the stellar ages and masses, the dynamical properties of both systems are robustly determined.

5.1 TIC 167692429

This triple has a mutual inclination of $i_{\rm m} \approx 27°$, which remains below the high eccentricity excitation Lidov–Kozai regime (i.e. $141° \gtrsim i_{\rm m} \gtrsim 39°$; see e.g. Lidov 1962; Kozai 1962; Naoz 2016) and excites only small, but rapid eccentricity oscillations with a full-amplitude of $\Delta e_1 \approx 0.05$ and a period of $P_{e_1} \approx 8000$ d. Therefore, one can conclude that the present configuration of the system is stable. We also confirmed this conclusion with a 10 million-year-long numerical integration, which did not show any dramatic variations in the orbital parameters. Therefore, we restrict our discussion only to some short-term, (partly) observational related facts. We plot the variations of some of the orbital elements during the first century of the recent millennium in the four panels of Fig. 10. Besides the above-mentioned cyclic, apse-node time-scale eccentricity variations, the spikes around the periastron passage of the outer orbit are also clearly visible (upper left panel). One can expect to detect these ~20-yr period eccentricity cycles via RV follow-up observations. Furthermore, the dominant dynamically forced apsidal motion is also clearly visible (upper right-hand panel). We plot the variations of both the observable arguments of

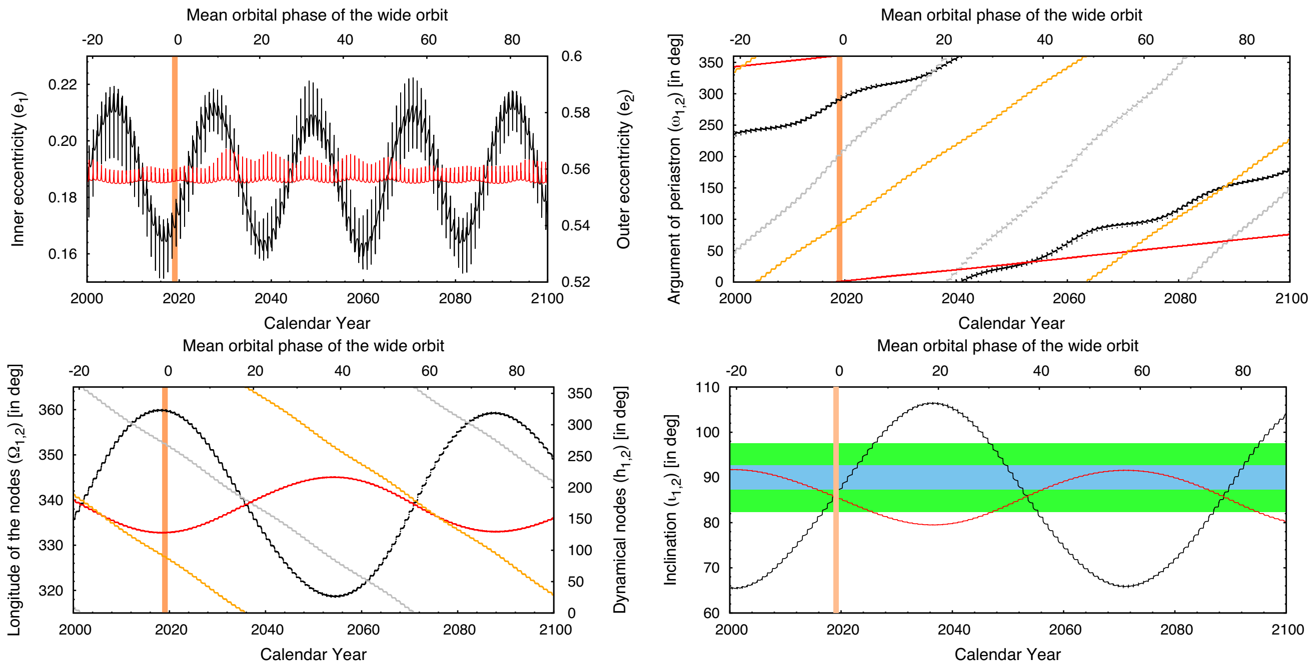

Figure 10. Variations of different instantaneous (osculating) orbital elements for TIC 167692429, obtained via numerical integrations. (The orbital elements were sampled nearly at the same orbital phases of the inner binary during each of its cycles.) The vertical orange shaded region in each panel marks the interval of the *TESS* observations. *Upper left, eccentricities:* Inner and outer orbits (black and red, respectively). *Upper right, arguments of periastron:* Observable (measured from the intersection of the tangential plane of the sky and the respective orbital plane) and dynamical (measured from the intersection of the two orbital planes) for the inner (black – observable; grey – dynamical) and outer orbits (red – obs.; orange – dyn., respectively). *Bottom left, longitudes of the nodes:* Observable (measured from an arbitrary starting point towards the intersection of the tangential plane of the sky and the respective orbital plane along the tangential plane of the sky) and dynamical (measured from the intersection of the invariable plane with the tangential plane of the sky toward the intersection of the two orbital planes along the invariable plane) for the inner (black – observable; grey – dynamical) and outer orbits (red – obs.; orange – dyn., respectively). *Bottom right, inclinations:* Inner and outer binaries (black and red curves, respectively). The wide green-shaded horizontal area denotes the inclination (i_1) domain of the inner binary where regular eclipses can occur. The narrower blue-shaded area stands for the outer inclination (i_2) domain for possible outer eclipses. (See the text for details.)

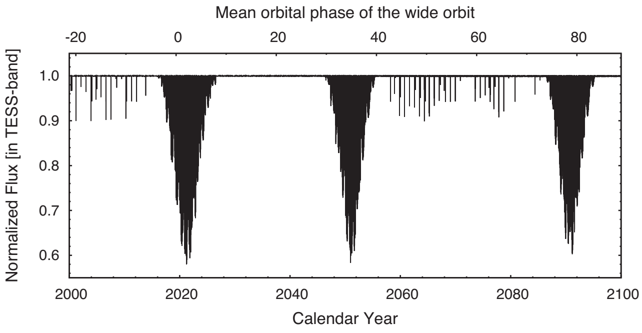

Figure 11. Photodynamical model light curve of TIC 167692429 for the first century of the present millennium. During one cycle of an ∼70- yr-long precession cycle there are two ∼11- yr-long intervals when the inner binary exhibits regular eclipses with continuously varying eclipse depths (marked as the densely packed black regions). Furthermore, interestingly, during the longer gaps (of about 40 years) between the regular binary eclipses, the system also exhibits outer eclipses, i.e. events when the outer, third star eclipses one or both members of the inner binary or, is eclipsed by them. These are seen as the more isolated dips spaced by about the outer orbital period of nearly a year.

periastron, i.e. the angle between the intersection of the respective orbital plane with the tangential plane of the sky, and the periastron point of the given orbit, and its dynamical counterpart, i.e. a similar angle measured between the intersection of the two orbital planes and periastron. While the former angles can be directly obtained from both RV measurements and ETV and light-curve analyses, the latter ones have an important role in the dynamical evolution of the system [see e.g. Borkovits, Forgács-Dajka & Regály (2007) and Borkovits et al. (2015) for a more detailed discussion about the different effects of the observable and dynamical arguments of periastrons and nodes].

As a consequence of their non-coplanarity, both orbital planes precess with a period of about $P_{\rm node} \approx 70$ yr. During this interval, the dynamical nodes regress by 360° on the invariable plane (see the bottom left-hand panel of Fig. 10), while the normals to the inner and outer planes move along cones with half angles equal to the dynamical inclinations ($i_{\rm dyn1,2} \approx 21^\circ$ and $\approx 6^\circ$, respectively) of the two orbits. The consequent variations of the observable inclinations are plotted in the bottom right-hand panel, while the most spectacular observational effect of this precession is shown in Fig. 11. Perhaps the most interesting feature of this triple is that, for the almost edge-on invariable plane ($i_{\rm inv} \approx 85.6^\circ$), the system is also subject to outer eclipses during certain intervals. Interestingly, by chance, the intervals of the regular inner, and the more or less random outer, eclipses do not overlap each other. The last period of outer eclipses has ended in 2014 just 1 yr before the start of the recent inner eclipsing episode at the end of 2015. Similarly, the forthcoming outer eclipse is expected in 2056, while the next cycle of regular, inner eclipses is predicted to finish in 2055.

Realizing that, according to our photodynamical solution, the target might have produced outer eclipses during the interval of the WASP observations we checked the photodynamical model light curve against the WASP observations. In Fig. 12, we plot the (1-h binned) WASP observations together with the photodynamical model. We found that all but the last outer eclipse during that interval fell into seasonal gaps (see the left-hand panel of Fig. 12). The last event, however, was found to be very close to the only extra dimming observed by the WASP cameras on the nights of 2012 March 12 and 13, which previously was thought to be an artefact. Therefore, as a very last step, we added the WASP light curve to the complex photodynamical, SED, and isochrone parameter search process, to refine our solution, and we were actually able to find sets of the initial parameters that led to solutions in accord with the location of the dimming observed by WASP (the right-hand panel of Fig. 12).

Note, however, that our extended MCMC runs in this last stage were unable to reproduce the depth of this extra dimming event perfectly. All the accepted model parameter sets resulted in a systematically shallower extra eclipse with a discrepancy of ∼0.01–0.015 mag. This might result from slightly discrepant (i) model ratios of the stellar surface brightnesses; (ii) other parameters such as the size of star C (which was fully eclipsed by the inner binary during that event) relative to the A–B binary members; or (iii) some of the dynamical parameters that could result in somewhat inaccurately modelled orbital perturbations going back 6 yr. One should keep in mind, however, that there are only 6 points out of a total of ∼1700 light-curve points that were used in the light-curve modelling part of our fitting process. And, only these six points carry any direct information, for example, about the surface brightness and radius ratio of star C relative to the inner A-B binary members. Consequently, we cannot expect a perfect fit from such minimal information content. Despite this minor discrepancy, however, we can conclude, that the WASP observations confirm the former

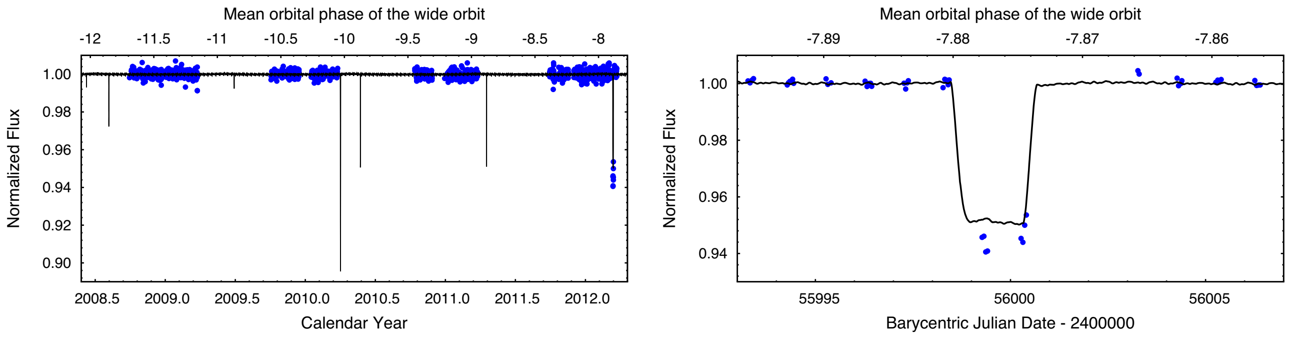

Figure 12. WASP observations of TIC 167692429 in 1-h bins (blue circles) together with the photodynamical model light curve (black line). It can clearly be seen in the *left-hand panel* that all but one of the outer eclipses are located within seasonal gaps of the WASP measurements. A zoom-in of the only extra dimming observed during the WASP measurements is shown in the *right-hand panel*. The corresponding section of the photodynamical model light curve confirms that this dip is probably a chance observation of an extra eclipse in this triple.

extra-eclipsing nature of our target and, of course, this fact makes our solution more robust.

5.2 TIC 220397947

In contrast to the system above, this target has shown constant eclipse depths not only during the 10-month interval of *TESS* measurements, but similarly deep regular eclipses were also observed continuously during the four seasons of the WASP observations. This fact suggests that the inner triple system should be very flat. Not surprisingly, our photodynamical model has resulted in a mutual inclination of $(i_{\rm mut})_{\rm AB\text{-}C} \approx 0.6^{\circ}$. On the other hand, however, as mentioned earlier, we found a clear discrepancy between the occurrence times of the WASP and *TESS* eclipses. In order to resolve this discrepancy, we assumed that TIC 220397947 is indeed an – at least – quadruple system with a hierarchical of 2+1+1 structure. The outermost orbital solution is, however, quite ambiguous and, even the presence of the fourth component remains questionable. Fortunately, apart from the time shift in the moments of the eclipses, the presence or absence of this low-mass stellar component affects only weakly both the present-day astrophysical and dynamical parameters of this system.

The situation is reminiscent of the case of the recently discovered quadruple system EPIC 212096658 (Borkovits et al. 2019b). That system consists of a similarly flat and compact ($P_2/P_1 = 59/2.9 \approx 20.3$ versus $P_2/P_1 = 77/3.6 \approx 21.4$, for the *K2* and *TESS* systems, respectively) inner triple subsystem, where the innermost EB is also formed by two stellar twins ($q_1 = 0.98$ versus 0.95), though the stars of the former EB themselves are significantly less massive. Moreover, both systems consist of nearly circular inner orbits. The fourth, outermost, less massive component of EPIC 212096658 was found through the systematic deviations in both the systemic RV of the triple system and the ETV residuals. In that case, however, the RV observations have covered more than 4.5 outermost orbital cycles and, therefore, the presence of the fourth star seems to be certain. In the present situation, future RV and/or eclipse timing observations are necessary to judge the four-body hypothesis and refine the orbital parameters of the widest orbit.

6 SUMMARY AND CONCLUSIONS

In this work, we have reported the discovery and complex analyses of the first two compact hierarchical triple star systems discovered with *TESS* in or near its southern continuous viewing zone during Year 1. Both TICs 167692429 and 220397947 were previously unknown EBs, and the presence of a third companion star was inferred from ETVs exhibiting signatures of strong third-body perturbations and, in the first system, also from eclipse depth variations. We carried out comprehensive analyses, including the simultaneous photodynamical modelling of *TESS* and archival ground-based WASP light curves, as well as ETV curves. Also, for the first time, we included in the simultaneous fits multiple star SED data and theoretical PARSEC stellar isochrones, taking into account *Gaia* DR2 parallaxes and catalogued metallicities.

TIC 167692429 is found to be an eccentric triple star system consisting of two *F*-type twin stars forming the inner binary ($P_1 = 10.26$ d, $e_1 = 0.17$; $q_1 = 0.99$), while the third, less massive G-type star is on a moderately mutually inclined and eccentric orbit ($P_2 = 331.5$ d, $e_2 = 0.56$, $i_{\rm mut} = 27^{\circ}$; $q_2 = 0.34$). Given the mutually inclined configuration, the binary orbital plane precesses with a period of $P_{\rm apse} \approx 70$ yr, causing ∼10-yr-long intervals where there are binary eclipses, interrupted by longer intervals with no binary eclipses, but during which irregular third-body outer eclipses are predicted. We identify one likely outer eclipsing event near the end of WASP observations in 2012.

In the absence of available RV and quantitative spectroscopic observations, we used theoretical stellar isochrones and SED data for constraining effective temperatures, masses, and other fundamental parameters of the stars being investigated. Our original idea was to obtain reliable stellar temperatures with a combination of (i) integrated SED information, (ii) photodynamically obtained mass ratios and relative stellar radii, and (iii) theoretical stellar isochrones. This process resulted in a multitude of stellar isochrones with different triplets of primary mass, age, and metallicity that were found to be consistent with the SED and the photodynamical light-curve solutions. Then, taking into account the accurate *Gaia* DR2 distances and auxiliary catalogued metallicities, we expected to find a proper narrow range of the appropriate isochrones that would be consistent with the astrometric distances to the systems. In turn, this would lead to accurate stellar masses as well as stellar ages, metallicities, etc. Unfortunately, however, we found that either the *Gaia* distances or the metallicities, or both are strongly inconsistent with the solutions we obtained.

For TIC 167692429, the present *Gaia* DR2 distance would imply unphysically large stellar masses for the appropriate stellar radii, effective temperatures, and metallicities. We interpret this inconsistency with the systematic effect of the almost 1-yr-period outer orbit on the trigonometric parallax measurements. As a consequence, in the present situation we are unable to obtain accurate stellar masses for this system and, furthermore, according to stellar isochrones TIC 167692429 might be either a very young [pre-main sequence (MS)] or old (evolved, post-MS) system. If some future RV observations produce dynamical masses, one will be able to decide whether the post- or the pre-MS scenario is valid. Furthermore, sufficiently accurate dynamical masses could be used to determine the metallicity as well as a more accurate photometric distance. In addition, after obtaining very accurate *Gaia* DR3 distances and spectroscopically obtained dynamical masses, this triple would be appropriate for high-accuracy testing of stellar isochrones.

In the case of TIC 220397947, this more compact coplanar triple has its binary formed by two *F*-type twins on an almost circular orbit ($P_1 = 3.55$ d, $e_1 = 0.001$; $q_1 = 0.95$), while the low-mass tertiary star has a rather short orbital period ($P_2 = 77.1$ d, $e_2 = 0.23$, $i_{\rm mut} = 0.6^{\circ}$; $q_2 = 0.25$). Archival WASP photometric observations reveal a discrepancy in the eclipse times that we interpret in terms of the presence of a fourth low-mass star in the system with an orbital period of $P_3 \approx 2700$ d. In the absence of RV observations, we were unable to calculate accurate masses and ages for the two systems. According to stellar isochrones, TIC 167692429 might be either a very young pre-MS or an old (evolved) post-MS system. In the case of TIC 220397947, our combined solution prefers a young pre-MS scenario.

Both triples are currently scheduled to be observed during the *TESS* extended mission. Similar to the Year 1 measurements, TIC 167692429 is likely to be observed in all but one of the Year 3 sectors. Our photodynamical model predicts the deepest eclipses within the present 11-yr-long cycle of regular eclipses during these observations.[11] This fact, combined with spectroscopic and RV measurements, not to mention the future orbital-motion-corrected

---

[11] Note, unfortunately, that the periastron passage of the outer orbit during that year and also the exact edge-on-view of the EB's orbital plane would

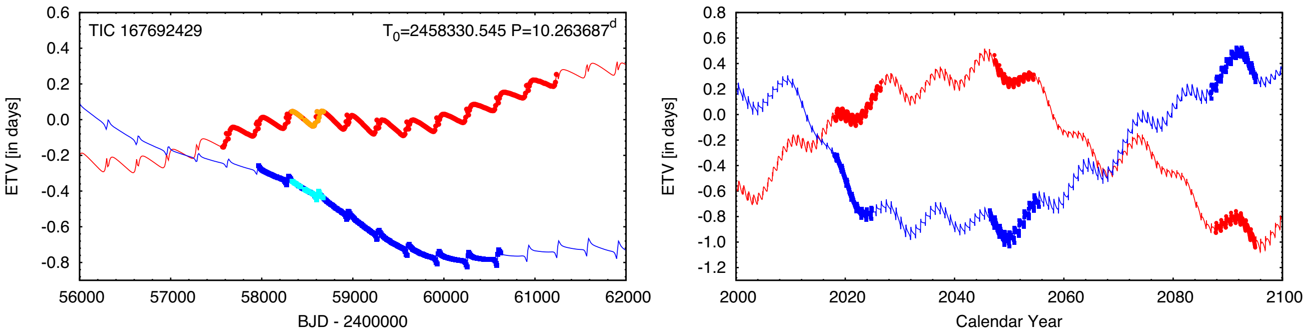

Figure 13. Eclipse and conjunction timing variations of the inner orbit of TIC 167692429 according to our photodynamical model on different time-scales during the twenty-first century. Conjunction times are for intervals without detectable eclipses; red and blue lines represent the inferior and superior conjunctions of the secondary component, respectively. During intervals of regular eclipsing, these lines are overplotted with heavier symbols corresponding to the primary (red) and secondary (blue) ETVs, also derived from the same model. Furthermore, in the left-hand panel the observed ETVs calculated from the eclipse observations of the *TESS* spacecraft are also plotted with orange and cyan dots. Besides the dynamically forced apsidal motion, additional quasi-cyclic effect of other secular third-body perturbations are also distinctly visible.

Gaia DR3 results, should offer extraordinarily accurate fundamental stellar parameters and orbital elements for this system. Furthermore, regular monitoring of the normal binary eclipses over the next few years, up to the conclusion of the present cycle of regular eclipses, would also allow us to detect not only the dynamically forced apsidal motion but also other kinds of secular three-body perturbations (see Fig. 13). Note that the amplitude and (quasi-)period of these secular (or, in the present context one might say, 'decadal') perturbations are very sensitive to the masses and the orbital configuration. Therefore, an accurate detection of these features may also lead to extremely accurate masses and other dynamical parameters.

TIC 220397947 is also expected to be re-observed in Year 3 Sectors 29–33, 35, 36, 38, and 39. These observations, hopefully, will either verify or reject the quadruple system hypothesis. Independent of this, RV observations of this very tight, relatively bright, SB2 system would also offer the same advantages as in the case of our other system, making this triple or quadruple also a benchmark system for stellar evolutionary tracks and isochrones.

ACKNOWLEDGEMENTS

TB acknowledges the financial support of the Hungarian National Research, Development and Innovation Office – NKFIH Grant KH-130372.

This project has been supported by the Lendület Program of the Hungarian Academy of Sciences, project no. LP2018-7/2019 and the MW-*Gaia* COST Action (CA 18104).

This paper includes data collected by the *TESS* mission. Funding for the *TESS* mission is provided by the NASA Science Mission directorate. Some of the data presented in this paper were obtained from the Mikulski Archive for Space Telescopes (MAST). STScI is operated by the Association of Universities for Research in Astronomy, Inc., under NASA contract NAS5-26555. Support for MAST for non-HST data is provided by the NASA Office of Space Science via grant NNX09AF08G and by other grants and contracts.

This work has made use of data from the European Space Agency (ESA) mission *Gaia*,[12] processed by the *Gaia* Data Processing and Analysis Consortium (DPAC; https://www.cosmos.esa.int/web/gaia/dpac/consortium). Funding for the DPAC has been provided by national institutions, in particular the institutions participating in the *Gaia* Multilateral Agreement.

This publication makes use of data products from the *WISE*, which is a joint project of the University of California, Los Angeles, and the Jet Propulsion Laboratory/California Institute of Technology, funded by the National Aeronautics and Space Administration.

This publication makes use of data products from the 2MASS, which is a joint project of the University of Massachusetts and the Infrared Processing and Analysis Center/California Institute of Technology, funded by the National Aeronautics and Space Administration and the National Science Foundation.

We used the Simbad service operated by the Centre des Données Stellaires (Strasbourg, France) and the ESO Science Archive Facility services (data obtained under request number 396301).

REFERENCES

Alonso R., Deeg H. J., Hoyer S., Lodieu N., Palle E., Sanchis-Ojeda R., 2015, A&A, 584, L8
Auvergne M. et al., 2009, A&A, 506, 411
Benedict G. F., McArthur B. E., Harrison T. E., 2018, RNAAS, 2, 22
Borkovits T., Csizmadia S., Forgács-Dajka E., Hegedüs T., 2011, A&A, 528, A53
Borkovits T., Forgács-Dajka E., Regály Z., 2007, A&A, 473, 191
Borkovits T., Hajdu T., Sztakovics J., Rappaport S., Levine A., Bíró I. B., Klagyivik P., 2016, MNRAS, 455, 4136
Borkovits T., Rappaport S., Hajdu T., Sztakovics J., 2015, MNRAS, 448, 946
Borkovits T., Sperauskas J., Tokovinin A., Latham D. W., Csányi I., Hajdu T., Molnár L., 2019b, MNRAS, 487, 4631
Borkovits T., Érdi B., Forgács-Dajka E., Kovács T., 2003, A&A, 398, 1091
Borkovits T. et al., 2019a, MNRAS, 483, 1934
Borucki W. J. et al., 2010, Science, 327, 977
Bressan A., Marigo P., Girardi L., Salasnich B., Dal Cero C., Claudia R., Rubele S., Nanni A., 2012, MNRAS, 427, 127
Castelli F., Kurucz R. L., 2004, preprint (astro-ph/0405087)
Collier Cameron A. et al., 2006, MNRAS, 373, 799
Cutri R. M. et al., 2013, wise.rept, 1C
Devor J., Charbonneau D., 2006, ApJ, 653, 647
Fabrycky D., Tremaine S., 2007, ApJ, 669, 1298
Ford E. B., Kozinsky B., Rasio F. A., 2000, ApJ, 535, 385
Gaia Collaboration et al., 2016, A&A, 595, A1

---

occur right during Sector 35 measurements when the triple will not be visible to the *TESS* cameras.

[12] https://www.cosmos.esa.int/gaia

Gaia Collaboration et al., 2018, A&A, 616, A1
Hajdu T. et al., 2017, MNRAS, 471, 1230
Hellier C. et al., 2011, in Bouchy F., Díaz R., Moutou C., eds, Detection and Dynamics of Transiting Exoplanets, EPJ Web of Conf., Vol. 11, EDP Sciences, p. 01004
Henden A. A., Levine S., Terrell D., Welch D., 2015, American Astronomical Society, AAS Meeting #225, id.336.16
Hippke M., David T. J., Mulders G. D., Heller R., 2019, AJ, 158, 143
Høg E. et al., 2000, A&A, 355, L27
Jordi C. et al., 2010, A&A, 523, A48
Kirk B. et al., 2016, AJ, 151, 68
Kozai Y., 1962, AJ, 67, 591
Lidov M. L., 1962, Planet. Space Sci., 9, 719
Loeb A., Gaudi B. S., 2003, ApJ, 588, L117
Lucy L. B., 1967, ZA, 65, 89
Maxted P. F. L., Hutcheon R. J., 2018, A&A, 616, A38
Moe M., Di Stefano R., 2013, ApJ, 778, 95
Moe M., Di Stefano R., 2015, ApJ, 810, 61
Moe M., Kratter K. M., 2018, ApJ, 854, 44
Naoz S., 2016, ARA&A, 54, 441
Oelkers R. J., Stassun K. G., 2018, AJ, 156, 132
Pollacco D. L. et al., 2006, PASP, 118, 1407
Prša A., Zwitter T., 2005, ApJ, 628, 426
Pál A., 2009, PhD thesis, Loránd Eötvös Univ.
Pál A., 2012, MNRAS, 421, 1825
Rappaport S., Deck K., Levine A., Borkovits T., Carter J., El Mellah I., Sanchis-Ojeda R., Kalomeni B., 2013, ApJ, 768, 33
Rappaport S. et al., 2017, MNRAS, 467, 2160
Ricker G. R. et al., 2015, JATIS, 1, 014003
Sharma S. et al., 2018, MNRAS, 473, 2004
Skrutskie M. F. et al., 2006, AJ, 131, 1163
Stassun K. G. et al., 2018, AJ, 156, 102
Tamuz O., Mazeh T., Zucker S., 2005, MNRAS, 356, 1466
Tokovinin A., 2019, AJ, 158, 222
Tokovinin A., Moe M., 2020, MNRAS, 491, 5158
van Kerkwijk M. H., Rappaport S., Breton R., Justham S., Podsiadlowski Ph., Han Z., 2010, ApJ, 715, 51
Windemuth D., Agol E., Ali A., Kiefer F., 2019, MNRAS, 489, 1644
Zahn J.-P., Bouchet L., 1989, A&A, 223, 112

This paper has been typeset from a TEX/LATEX file prepared by the author.